

PHD TUTORIAL

Discrete optics in femtosecond-laser-written photonic structures

To cite this article: Alexander Szameit and Stefan Nolte 2010 *J. Phys. B: At. Mol. Opt. Phys.* **43** 163001

View the [article online](#) for updates and enhancements.

You may also like

- [An Array Consisting of 10 High-Speed Side-Illuminated Evanescently Coupled Waveguide Photodetectors Each with a Bandwidth of 20 GHz](#)
Qian-Qian Lv, , Han Ye et al.
- [Integrated photonic quantum walks](#)
Markus Gräfe and Alexander Szameit
- [Proposal for calibration of a single-photon counting detector without the need of input photon flux calibration](#)
Thomas Gerrits



IOP | ebooks™

Bringing together innovative digital publishing with leading authors from the global scientific community.

Start exploring the collection—download the first chapter of every title for free.

PhD TUTORIAL

Discrete optics in femtosecond-laser-written photonic structures

Alexander Szameit¹ and Stefan Nolte²

¹ Physics Department and Solid State Institute, Technion, 32000 Haifa, Israel

² Institute of Applied Physics, Friedrich-Schiller-Universität Jena, Max-Wien-Platz 1, D-07743 Jena, Germany

E-mail: Szameit@techunix.technion.ac.il

Received 9 March 2010, in final form 2 June 2010

Published 23 July 2010

Online at stacks.iop.org/JPhysB/43/163001

Abstract

Over the last few years arrays of evanescently coupled waveguides have been brought into focus as a particular representation of functionalized optical materials, in which the dispersion and diffraction of propagating light can be specifically tuned. Moreover, it turns out that the light evolution in these systems shares fundamental similarities to the quantum evolution of particle wavefunctions, so that waveguide arrays can act as a model system for emulating quantum mechanics. Recently, a novel technique was developed with which waveguides can be directly ‘written’ into various optical bulk materials using femtosecond laser pulses, which allows for the realization of a variety of innovative concepts which are not feasible using other fabrication methods. The aim of this tutorial is to give an introduction to this topic.

(Some figures in this article are in colour only in the electronic version)

Introduction

Discreteness is an important aspect in a variety of research fields in modern physics. The atomistic structure of matter in solid-state physics and the discrete nature of electromagnetic phenomena in quantum mechanics are only two popular examples for the fundamental role that discreteness plays today. Yet many of the theoretical predictions obtained in these fields of research are often hard to verify experimentally. However, discrete phenomena of distinct origin, e.g. in Bose–Einstein condensates (BECs) and electronic crystals, are very often strongly related, since they can be described as a coherent interaction of a number of discrete cells. Such equivalent physical systems exhibiting similar structures in the mathematical formalism provide the possibility of verifying experimentally a variety of effects. Here, arrays of evanescently coupled waveguides, featuring an inherent breaking of the isotropy of space, are one of the most prominent systems [1], since they allow for a direct visualization of the evolution of the wavefunction. The structure of the underlying mathematical apparatus suggests that due to obvious symmetries in the governing equations, most of

the results can be applied to discrete systems in general. Hence, the experimental demonstration of discrete phenomena in waveguide arrays reveals the fundamental properties of discreteness in general. Accordingly, in recent decades the investigation of light propagation in waveguide lattices has been a steadily growing field of interest. However, when the field advanced, many of the observed phenomena became rather ‘optical’, since they often had no direct analogue in any other field of physics. This indicates that lattices of evanescently coupled waveguides are not just a simple model system for a comparative investigation of discreteness, but constitute a unique discrete physical system on their own as well [2]. After being limited for years to one-dimensional (1D) configurations, the research in waveguide arrays grew to new heights when two-dimensional (2D) lattices were experimentally realized in 2003, using optical induction in photorefractive crystals [3, 4]. This was the initial point for extensive theoretical and experimental research also in 2D discrete optics since, naturally, in such structures more complex phenomena can be generated (e.g. vortex solitons; see [5] for an extended review).

However, the postulation of numerous discrete optical concepts relying on boundaries and interfaces in finite 2D lattices and lattices with specifically tailored properties (for a summary of such effects see [5]) revealed strong limitations of the available techniques with respect to the fabrication of waveguide arrays with specifically tailored shapes and functionalities in one and two dimensions. The experimental demonstration of these new ideas requires a high degree of freedom in the lattice topology and, furthermore, precise control of the properties of every single waveguide, so that highly defined evanescent coupling and in particular artificial defects in the lattice can be realized. It became evident that a new approach for the experimental realization of such structures was required.

In 2004, waveguide arrays fabricated by the femtosecond (fs) direct-writing method were demonstrated for the very first time [6, 7]. This technique offers a versatile method for the fabrication of waveguide arrays with distinct properties and features. Since then, a variety of publications based on this approach dealt with numerous aspects of physics, from purely optical effects, quantum-optical analogues, integrated optical telecommunication devices to solitons and related nonlinear phenomena. In this tutorial, the underlying principles of discrete light propagation in fs-laser-written waveguide arrays are reviewed and recent achievements highlighted.

Discrete systems and arrays of evanescently coupled waveguides

The two most prominent examples of discrete systems in physics are without any doubt BEC in periodic optical potentials and, of course, the atomic structure of solids with their crystalline potential (figures 1(a) and (b)). Although discreteness obviously manifests itself in very distinct forms, the spirit of the underlying mechanisms of the dynamics is similar in every representation. In an abstract picture, in contrast to continuous systems, discrete systems consist of finite-sized, so-called discrete basic elements which interact with each other (figure 1(c)). The response of the discrete system depends therefore on the specific type of excitation, the individual properties of the basic elements and their interaction. Every setting which belongs to the class of systems exhibiting this specific characteristic may hence be called ‘discrete’. As a consequence, it is feasible to project phenomena, commonly associated with a particular discrete system, to an apparently different system, where they are possibly much easier accessible and observable. The results may then be generalized to all discrete systems.

In recent years it turned out that weakly guiding and evanescently coupled photonic waveguide structures provide an excellent model system for the analysis of the characteristics of discrete systems [1] (figure 1(d)). This becomes particularly clear when one compares the Schrödinger equation describing the dynamics of the wavefunction Ψ in a variety of quantum-mechanical settings:

$$i\hbar \frac{\partial}{\partial t} \Psi(x, y, t) = - \left(\frac{\hbar^2}{2m} \left[\frac{\partial^2}{\partial x^2} + \frac{\partial^2}{\partial y^2} \right] - V(x, y, t) \right) \Psi(x, y, t) \quad (1)$$

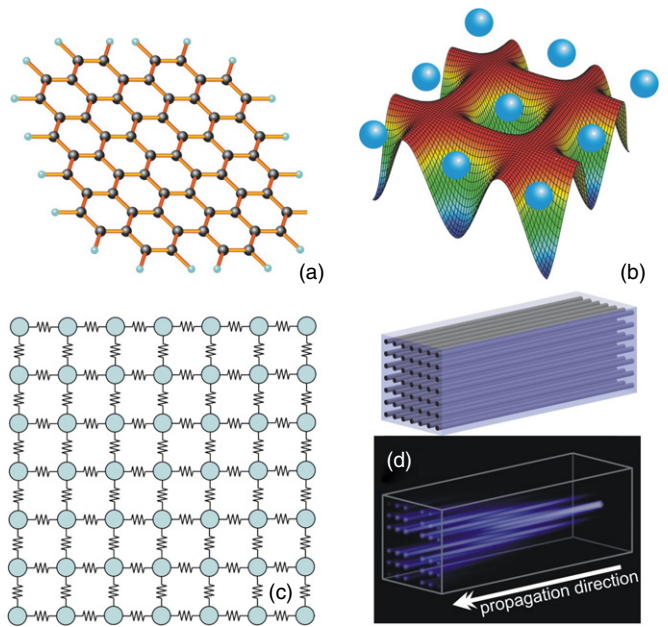


Figure 1. Discrete systems in physics. (a) Solid with its crystalline potential. (b) BEC in an optical lattice (image courtesy of Rolston group, University of Maryland). (c) The general scheme: individual elements are connected by their interaction. (d) Arrays of evanescently coupled waveguides as an optical version of a discrete system.

and the optical paraxial Helmholtz equation for the evolution of the electrical field envelope E :

$$i\lambda \frac{\partial}{\partial z} E(x, y, z) = - \left(\frac{\lambda^2}{2n_0} \left[\frac{\partial^2}{\partial x^2} + \frac{\partial^2}{\partial y^2} \right] + \Delta n(x, y, z) \right) E(x, y, z). \quad (2)$$

The equivalence is evident when the correspondence between the characteristic values is borne in mind: time t and distance z , Planck’s constant $\hbar = h/2\pi$ and reduced wavelength $\lambda = \lambda/2\pi$, mass m and refractive index of the bulk n_0 , and potential V and refractive index change $\Delta n = n_0 - n(x, y, z)$. Thereby the main advantage of optical systems is that the evolution of the wave packet takes place in space (evolution coordinate z) instead of time (evolution coordinate t). This allows for a direct observation by monitoring the spatial light propagation and prevents the need for resolving the very short time scales typically involved in the evolution of the electron probability wavefunction.

In a continuous medium, a light beam experiences normal diffraction and always spreads during propagation (figure 2(a)). This changes strongly when the index of refraction is periodically modulated [8, 9] (figure 2(b)). Most evident are the two strong side lobes, which confine a strongly modulated intensity pattern. Light is attracted by the increased index and stays during propagation in the vicinity of these regions, which accordingly act as waveguides. Along the transverse dimensions, the light is mainly found at these distinct points, supporting the term ‘discrete’ for this system. However, the evolving field is not entirely localized in the individual guides but spans an extended area

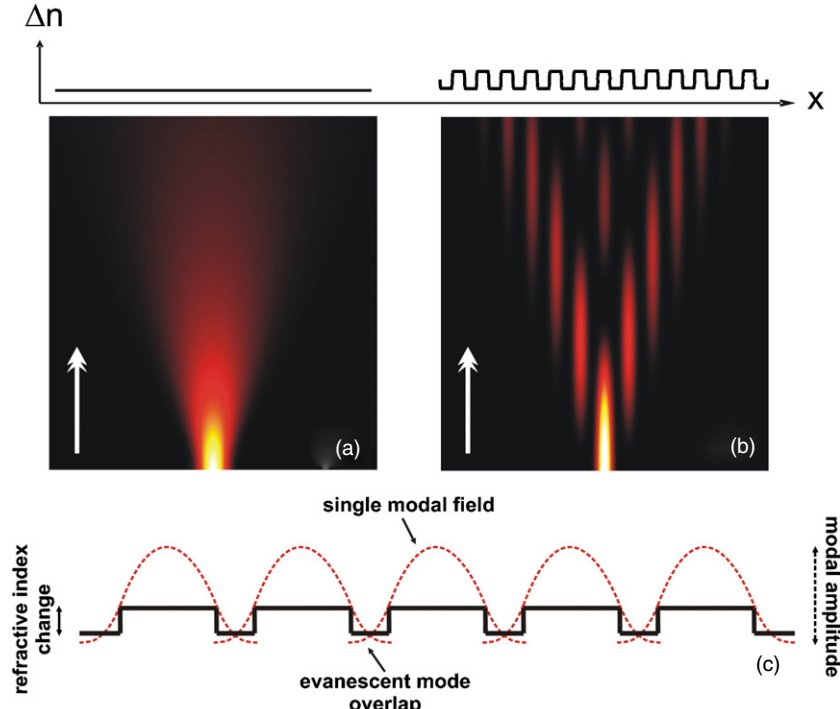


Figure 2. Discreteness impacts the light evolution. (a) Beam diffraction in a continuous medium. (b) Beam diffraction in a medium with periodically changing refractive index. (c) Sketch of a waveguide array. The modal fields of the individual guide overlap, which causes an energy transfer between adjacent guides.

with evanescent tails. Hence, the field in every guide is perturbed by its neighbours, which causes an energy flow, also known as evanescent coupling, from one waveguide to adjacent guides (figure 2(c)). In contrast to continuous media, where all three spatial dimensions are intrinsically equivalent, there is a fundamental difference between the longitudinal propagation direction z and the transverse directions x, y in which the energy transport occurs only by evanescent fields. This is why the characteristics of the field propagation and the resulting intensity distributions in the array are so fundamentally different in waveguide arrays compared to homogeneous media. This phenomenon is most obvious in the band structure, also known as the dispersion relation, of waveguide arrays, which connects the transverse β_x, β_y and longitudinal β_z wavevector components for a fixed optical frequency. In a homogeneous medium, assuming paraxiality, the dispersion relation reads

$$\beta_z = \beta_0 - \frac{\beta_x^2}{2\beta_0} - \frac{\beta_y^2}{2\beta_0} \quad (3)$$

and is shown for the 1D case in figure 3(a). However, in a waveguide lattice, for some transverse wavevectors the periodic refractive index acts as a Bragg grating. As a consequence, the continuous band is deformed and breaks at the critical angles, which define the Brillouin zones [10] (shown for a 1D array in figure 3(b)). In figure 3(c) the reduced band structure with the allowed propagation bands, separated by photonic bandgaps, is shown. This feature further emphasizes the close relation between different discrete systems such as solids and waveguide arrays, both exhibiting a band structure due to their intrinsic periodicity.

In order to describe the light evolution in evanescently coupled wave-guiding structures, one commonly employs the principle of coupled modes, in which the transverse shape of the modes in the individual guides is assumed to remain constant, so that only the amplitudes evolve. Since the interaction between the waveguides drops exponentially with increasing spacing, only coupling to the nearest lattice sites is taken into account. A separation of variables yields the coupled mode equations for the amplitude $\varphi_{m,n}$ in the m, n th waveguide [11]

$$i \frac{\partial \varphi_{m,n}}{\partial z} + \sum_{\mu, v=-1}^1 c_{\mu, v} \varphi_{m+\mu, n+v} = 0 \quad (4)$$

with the coupling coefficients (see figure 4(a))

$$c_{\mu, v} = \frac{\omega \varepsilon_0}{4} \iint_{x,y} [\Delta n(x, y)]^2 e_{m,n} e_{m+\mu, n+v} dx dy \quad (5)$$

quantifying the evanescent overlap between the transverse field components of the modes in adjacent guides. The quantity $e_{n,m}$ denotes the transverse field envelope in the m, n th guide, whereas ω is the optical frequency and ε_0 is the dielectric constant. Note that the self-coupling $c_{0,0}$ is commonly removed by normalization ($c_{0,0} \sim 0$). The coupling coefficients denote the energy flow from one waveguide to its neighbours. Due to energy conservation, one additionally finds $c_{\mu, v} = c_{-\mu, -v}$. Equation (4) applies on the most general case of a square lattice with diagonal coupling (figure 4(a)); hence, for less complex settings some of the $c_{\mu, v}$ vanish. In particular for a hexagonal structure (figure 4(b)), $c_{1,-1} = c_{-1,1} = 0$.

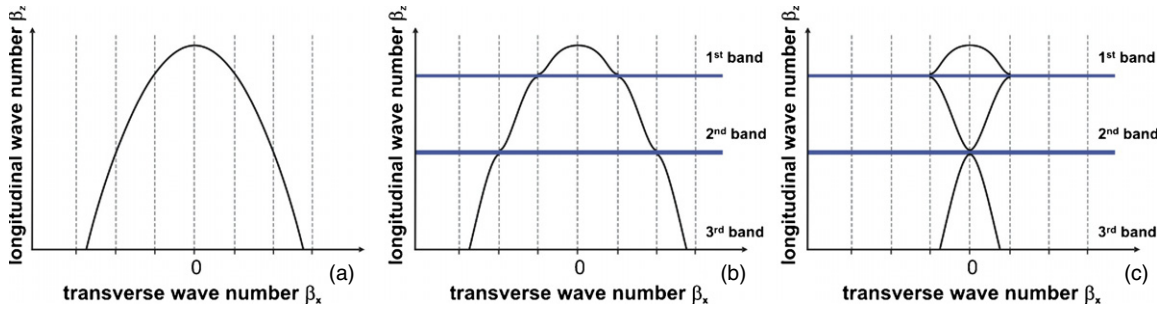


Figure 3. Band structures in waveguide arrays. (a) Dispersion relation of an isotropic medium in the paraxial approximation. (b) Dispersion relation of a discrete waveguide lattice. At the edge of the Brillouin zone, Bragg reflection occurs, yielding an anomalous bending of the dispersion relation and the formation of bandgaps, shown as blue regions. (c) Band structure of a waveguide lattice folded into the first Brillouin zone.

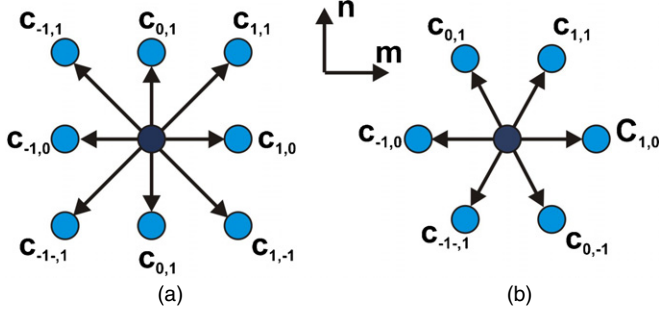


Figure 4. The unit cell with the coupling coefficients in 2D waveguide arrays. (a) In a square lattice with diagonal coupling, one has eight neighbours. (b) In a hexagonal lattice, one has six neighbours.

It is important to note that the coupled mode approach used to derive the basic equations of propagation is a paraxial approximation and, furthermore, only valid in the first propagation band. This approach, although intuitive, suffers from a lack of generality. A more universal approach, in which waveguide arrays are regarded as an example of a general 1D periodic optical structure, is the Floquet–Bloch analysis [10, 12]. It directly predicts that the spectrum of the propagation constants is divided into bands, separated by gaps, in which propagating modes do not exist. However, in most relevant cases the coupled mode approach is fully adequate, describing all of the observed propagation effects.

In order to get an intuitive picture of light propagation in waveguide arrays, it is instructive to derive an expression for the first propagation band, shown in figure 5(a). To this end, we consider a planar (1D) array $i\partial_z\varphi_m = -c(\varphi_{m+1} + \varphi_{m-1})$ and substitute the plane wave solutions

$$\varphi_m = \varphi_0 \exp\{i(\beta_m d + \beta_z z)\} \quad (6)$$

with the (discrete) transverse wavevector β_m in the transverse coordinate $md (= x)$, and the waveguide spacing d . This yields the dispersion relation

$$\beta_z = 2c \cos\{\beta_m d\}, \quad (7)$$

connecting the transverse and longitudinal dynamics. Obviously this relation is periodic, in contrast to equation (3) for the homogeneous medium. When an optical field propagates over a distance z , each transverse component gains a phase $\Phi = \beta_z(\beta_m)z$. The corresponding transverse shift of a wave centred around β_m is then $\Delta x = \partial\Phi/\partial\beta_m = (\partial\beta_z/\partial\beta_m)z$. Hence, the angle θ of propagation reads [8, 13]

$$\frac{\partial\beta_z}{\partial\beta_m} = \frac{\Delta x}{z} = \tan\theta. \quad (8)$$

For a 1D lattice, this results in the expression (see figure 5(b))

$$\frac{\partial\beta_z}{\partial\beta_m} = -2dc \sin\{\beta_m d\}. \quad (9)$$

Therefore, in the centre ($\beta_m d = 0$) and the edge ($\beta_m d = \pi$) of the Brillouin zone the angle of propagation is $\theta = 0$, whereas at $\beta_m d = \pi/2$ the angle $\theta = \text{atan}\{-2dc\}$.

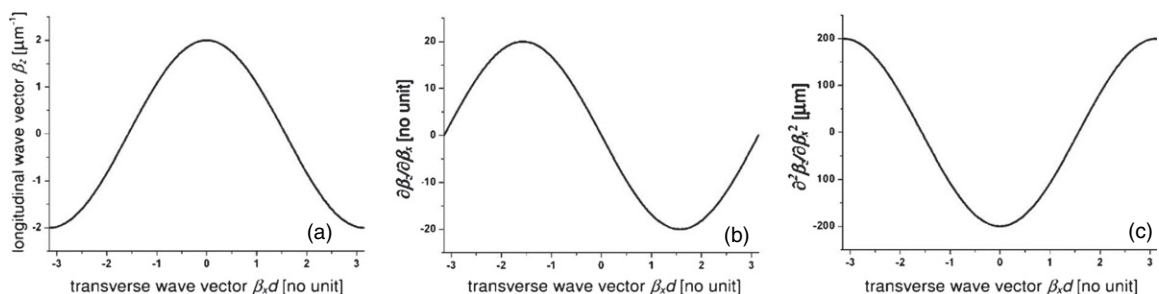


Figure 5. Anomalous refraction and diffraction in 1D waveguide arrays. (a) The dispersion relation $\beta_z(\beta_x)$. (b) The first derivative $\partial\beta_z/\partial\beta_x$, giving the direction of the beam. (c) The second derivative $\partial^2\beta_z/\partial\beta_x^2$, representing the diffraction strength. Note the vanishing diffraction at $\partial\beta_x = \pi/2$.

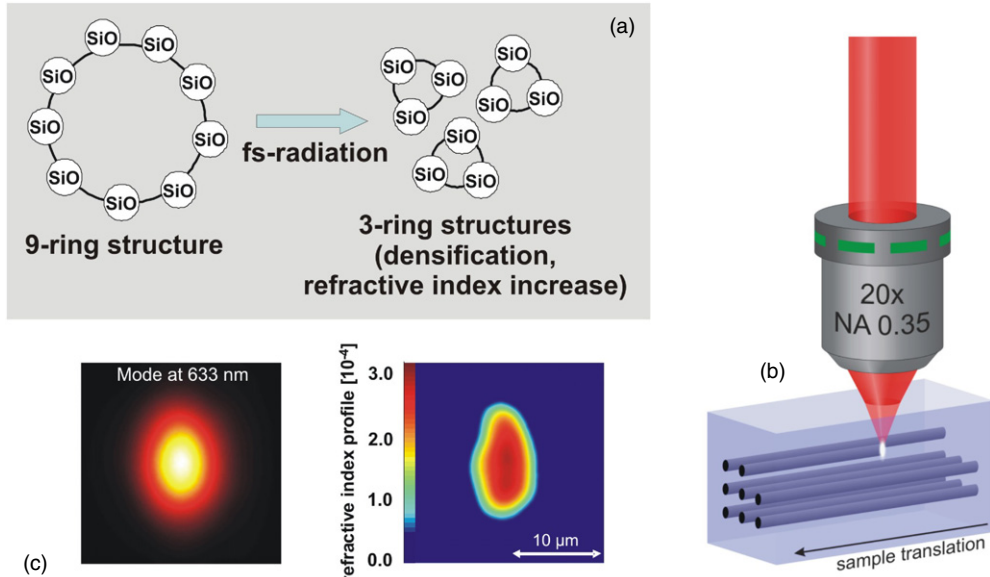


Figure 6. Writing waveguides in fused silica using fs laser pulses. (a) In the focal region of the writing objective, the high light intensities partially break the silica bonds. After reorientation this results in densification and a locally increased refractive index. (b) Moving the sample transversely to the beam results in an elongated index increase: a waveguide is created. (c) The guided mode at $\lambda = 633$ nm (left) and the cross section of the refractive index distribution (right) of an individual waveguide.

As a consequence, discrete systems exhibit a periodic anomalous refraction, which oscillates with increasing transverse wavenumber components. This behaviour is in strong contrast to homogeneous media, where the refraction is steadily increasing with increasing input angle.

Diffraction is caused by different transverse wavenumbers resulting in different propagation angles θ , yielding a spatial dispersion of different plane wave components. Therefore, the degree of diffraction can be determined by

$$\frac{\partial^2 \beta_z}{\partial \beta_m^2} = -2d^2 c \cos\{\beta_m d\}, \quad (10)$$

which is shown in figure 5(c). Whereas in homogeneous media diffraction is normal, in discrete waveguide lattices the behaviour is completely different since diffraction is periodic with positive and negative values. Accordingly, at specific transverse wave components (e.g. $\beta_m d = \pi/2$), diffraction completely vanishes.

Femtosecond-laser-written waveguide arrays: fabrication and characterization

For the detailed investigation of all aspects of discrete light propagation, waveguide lattices have to meet a variety of conditions. The coupling between the single lattice sites has to be highly homogeneous to prevent statistical and chaotic behaviour. Furthermore, the properties of every single waveguide should be tuneable, which in particular allows for the insertion of artificial defects. Moreover, a diversity of topologies has to be realizable in order to investigate the light evolution in one- and two-dimensional periodic lattices as well as in non-periodic configurations such as waveguide crossings and junctions. Additionally, the fabricated arrays should be stable and permanent. It turns out that the fs laser

writing technique is an excellent approach to fulfilling these requirements.

When ultrashort laser pulses are tightly focused into the bulk material, nonlinear absorption takes place leading to optical breakdown and the formation of a micro plasma, which induces a permanent change in the material's molecular structure. In the particular case of fused silica as the processed material, the density is locally increased [14], yielding an increase of the refractive index [15]. This phenomenon is commonly explained by the fact that bulk fused silica consists of molecular ring structures which are composed of several SiO_2 molecules each, which are partially broken by the fs laser radiation (see figure 6(a)). Subsequent recombination to smaller ring structures which are composed of less SiO_2 molecules with a higher packing density yields to the observed densification and, hence, to a local increase of the refractive index. When the spherical aberrations caused by the sample surface are small, the dimensions of these induced changes are approximately given by the size of the focal region of the writing objective and can be calculated using

$$w_0 = M^2 \frac{\lambda}{\pi \text{NA}}, \quad b = M^2 \frac{\lambda}{\pi \text{NA}^2}. \quad (11)$$

Here w_0 is the FWHM (full width at half maximum) radius of the focal spot and b is the Rayleigh length. M^2 characterizes the difference between a real laser beam and a diffraction-limited Gaussian beam, while NA is the numerical aperture. By moving the sample transversely with respect to the beam a continuous modification is obtained and a waveguide is created [16]. Such a guide can be written along arbitrary paths since the only limiting factor in the placement of the focus is the focal length of the writing objective [17]. Furthermore, all structural changes are permanent and stable after fabrication.

Writing waveguides is a very active field of research. Main topics are thereby on using a variety of bulk media

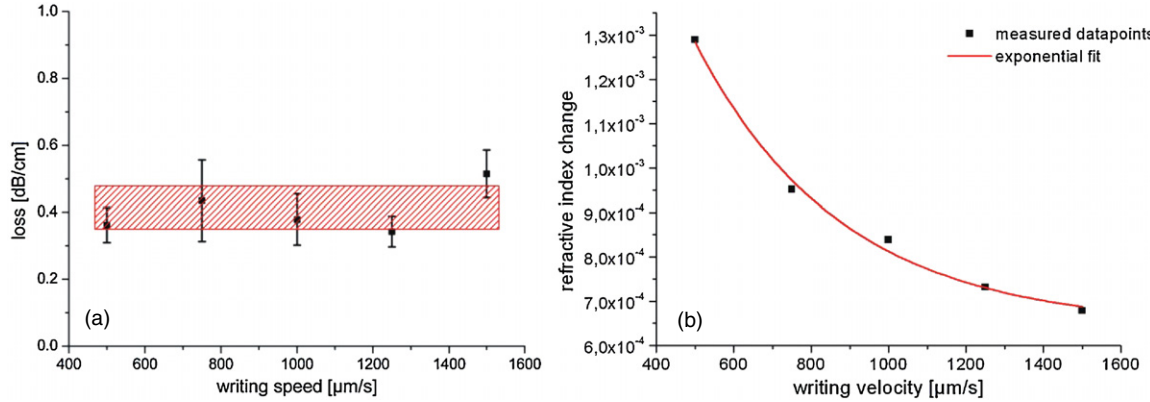


Figure 7. Characteristics of fs-laser-written waveguides. (a) The losses are approximately independent from the writing speed. (b) The refractive index change is a function of the writing speed. Figures from [23].

and on directly influencing the refractive index distribution of individual guides by beam shaping, minimizing propagation losses, detailed analysis of the multiple fabrication parameters, and more. We refer the interested reader to recent reviews on this topic and the references therein [18–21].

The waveguides used for the experiments presented in this tutorial were usually fabricated by a Ti:Sapphire laser system (RegA/Mira, Coherent Inc.) with a repetition rate of 100 kHz at a laser wavelength of 800 nm. The beam was typically focused into polished fused-silica samples by a 20× microscope objective with a numerical aperture of 0.45. This relatively low focusing ensures that the created refractive index change is almost independent of the writing depth inside the material, so even large waveguide structures are still homogeneous in the vertical dimension. A sketch of the writing setup is shown in figure 6(b). The resulting refractive index change (for a fixed polarization) can be obtained from the near-field distributions of the waveguides by calculating the inverse Helmholtz equation [22]

$$n^2(x, y) = n_{\text{eff}}^2 - \lambda^2 \frac{\Delta A(x, y)}{A(x, y)}, \quad (12)$$

using the assumption $n_{\text{eff}} = n_{\text{bulk}}$, where $A(x, y)$ is the intensity distribution of the fundamental mode at the output facet. A typical near-field pattern of a waveguide and the corresponding refractive index distribution obtained by using equation (12) are shown in figure 6(c).

The guiding properties of the individual waveguides are strongly dependent on the writing parameters. Within the multi-dimensional parameter space, the pulse duration, pulse energy and writing velocity are the key parameters influencing the resulting refractive index distribution. The optimal processing parameters with respect to the described setup are a pulse duration of about 150 fs and a pulse energy of 0.3 μJ [23]. Keeping these parameters fixed, by only changing the writing velocity v a specific tuning of the refractive index modulation is achieved. It could be shown that for writing velocities of about $500 \mu\text{m} < v_{\text{writing}} < 1500 \mu\text{m}$ the waveguide losses, measured by a cut-back method, are approximately constant (see figure 7(a)). However, the refractive index modulation decreases for increasing writing velocities due to the smaller overlap between successive pulses, as shown in figure 7(b).

This can be used for the modification of the guided modes, since for smaller refractive index changes the mode is less well guided resulting in a larger evanescent field. According to equation (5), this is directly related to the evanescent coupling between two waveguides, which is determined by the overlap of the evanescent fields of the waveguide modes allowing the tuning of the coupling not only by the waveguide separation but also by the writing velocity. This can be used for several applications but in particular to specifically introduce defects in a waveguide array with constant waveguide spacing.

As a particular feature, the light intensity distribution can be directly monitored inside the samples using a fluorescence microscopy technique [24, 25]. To this end a special type of fused silica with a high content of OH was used (Suprasil 311). During the writing process non-bridging oxygen hole centres (NBOHCs) are generated due to breaking of the molecular bonds. The NBOHCs have a broad absorption band around 2.0 eV [26] and exhibit an absorption maximum at 620 nm [27]. Hence, when launching red light from a HeNe laser at $\lambda = 633 \text{ nm}$ (corresponding to 1.95 eV) into the waveguides, these colour centres are excited and the resulting fluorescence (at $\lambda = 650 \text{ nm}$) can be directly observed. Since the colour centres are formed exclusively inside the waveguides, this technique yields a high signal-to-noise ratio. In contrast to fluorescent polymers (see e.g. [28]), the bulk material causes almost no background noise. The experimental setup is sketched in figure 8(a). The laser beam is launched into the waveguide array using a 10× microscope objective (NA = 0.25). The fluorescence distribution representing the diffraction pattern is imaged onto a CCD camera using a 5× objective (NA = 0.13). Most of the scattered HeNe-laser light is blocked by a 650 nm longpass filter which improves the image quality considerably. The electronic noise of the camera is suppressed by averaging over several (usually ten) images. The waveguide arrays have a very high length-to-width aspect ratio with sample lengths of up to 100 mm and lattice widths in the order of a few hundred microns. To overcome the problem to visualize a lattice with such a high length-to-width aspect ratio, while maintaining a high spatial resolution, the camera is translated along the sample and multiple images are recorded, scaled down to 20 pixels in the propagation direction and stitched together

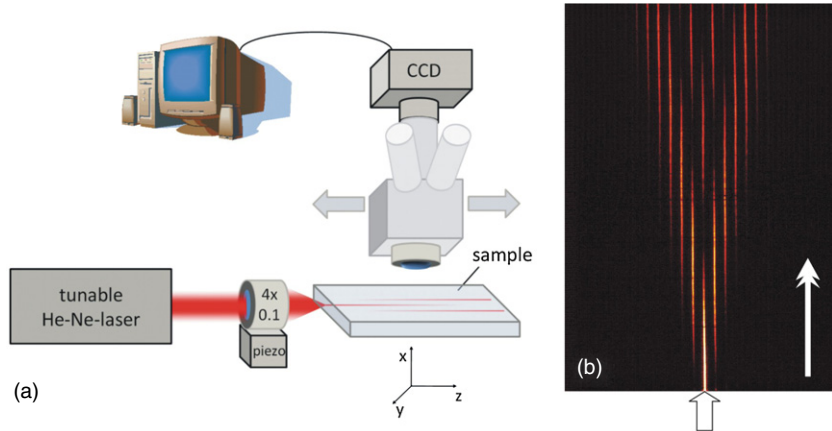


Figure 8. Fluorescence microscopy. (a) Experimental setup to observe the fluorescence radiation. (b) Observed fluorescence pattern of a straight waveguide array.

yielding images with a resolution of $40 \mu\text{m} \times 0.5 \mu\text{m}$ per pixel. Additionally, the propagation losses in the samples are removed by rescaling. For this purpose, the light propagation in a single waveguide is monitored and the recorded intensity is fitted with an exponentially decaying function, which is used to normalize the fluorescence images. In figure 8(b), a fluorescence microscope image of light propagation in a waveguide array after a single waveguide excitation is shown. Importantly, the dependence of the fluorescence intensity on the intensity of the propagating light is approximately linear, so that not only qualitative but also quantitative measurements can be performed.

Quantum-optical analogies

From the early days of quantum mechanics, the study of the electronic probability wavefunction in periodic lattices was of high interest for the scientific community. Particular attention was thereby paid to the investigation to the time-dependent evolution and the impact of external fields. It was shown by Felix Bloch in 1928 [29] that a linear transverse potential yields a periodic oscillation of the wavefunction. However, it took almost 65 years to experimentally observe such Bloch oscillations [30] by replacing the atomic lattice with a semiconductor superlattice. The challenge was to overcome the limit of a short electron coherence lifetime, which is lower than the oscillation time scale [1] of 40 ps for an atomic lattice period of 10 Å and an electric field strength of 10^6 V m^{-1} [31]. Hence, it seemed much more feasible to search for an analogue and to use an artificial lattice. It becomes apparent that the direct access to quantum effects is very intricate in many cases, requiring model systems in which the fundamental characteristics of the phenomenon under investigation can be adequately analysed.

Due to the similarity of the Schrödinger equation (1) and the paraxial Helmholtz equation (2), waveguide arrays provide an exceptional model system since the wave dynamics are the same in both systems. A main advantage is that in optics the evolution takes place in space instead of time, so the temporal evolution is mapped onto a spatial dimension (the propagation

direction) and can therefore be directly observed at an arbitrary resolution. Thus, even fast dynamic processes can be monitored in a static manner by applying available imaging techniques. Employing a constant transverse electrical field $\Sigma(z)$ on a particle with the charge q , the Schrödinger equation reads

$$i\hbar \frac{\partial}{\partial t} \Psi(x, y, t) = -\left(\frac{\hbar^2}{2m} \left[\frac{\partial^2}{\partial x^2} + \frac{\partial^2}{\partial y^2} \right] - V(x, y, t) + q\Sigma(z) \right) \Psi(x, y, t). \quad (13)$$

In the optical setting, the transverse force $q\Sigma(z)$ is equivalent to a detuning of the local refractive index of the waveguides. However, in order to realize proper conditions for the wave packet evolution, these index modifications have to be very precise which is intricate in the fabrication. Luckily, there is a much more sophisticated way to impose transverse gradients on the waveguide array, employing a curvature of the individual waveguides [32]. Assuming the bending to be much smaller than the waveguide spacing d , in the 1D case the paraxial Helmholtz equation (2) converts into

$$i\lambda \frac{\partial}{\partial z} E(x - x_0(z), z) = -\left(\frac{\lambda^2}{2n_0} \frac{\partial^2}{\partial x^2} + \Delta n(x - x_0(z)) \right) \times E(x - x_0(z), z), \quad (14)$$

where the longitudinal bending of the waveguides is described by $x_0(z)$. After transforming into the local coordinates $z \rightarrow z'$ and $x - x_0 \rightarrow x'$ and applying a Gauge transformation (for more details, see [25, 33]) one obtains

$$i\lambda \frac{\partial}{\partial z} E(x', z') = -\left(\frac{\lambda^2}{2n_0} \frac{\partial^2}{\partial x'^2} + \Delta n(x') - \ddot{x}_0(z')x' \right) E(x', z'). \quad (15)$$

The term \ddot{x}_0x' , where the dots stand for the derivative with respect to z' , acts now as the transverse force. Figure 9 gives an intuitive picture of the underlying physics. Let us assume a plane wave travelling through the array. In a straight array the plane wave does not change during propagation (figure 9(a)). If the waveguides are slightly curved, the plane wave will still propagate straight, being almost not affected by the bending

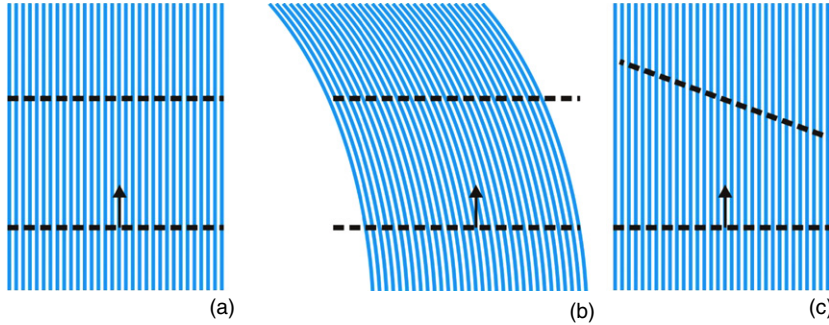


Figure 9. Plane wave evolution in a curved lattice. (a) In a straight lattice, a plane wave travels through the array without distortion. (b) In a slightly curved array, the plane wave still travels straight in the laboratory system. However, the path lengths differ for different waveguides. (c) In a curvilinear coordinate system where the waveguides appear straight, the plane wave exhibits a speed dependent on the position, causing an effective change of the refractive index.

(figure 9(b)). However, the arc length which is passed by the plane wave is now a function of the position of the individual guides. In the particular example of figure 9(b), the passed arc length of the outer left guide is larger than the arc length of the outer right guide. This is most apparent in the corresponding curvilinear coordinate system, where the waveguides appear to be straight. Owing to the geometrical effect, the plane waves seem to have travelled different distances, resulting in different effective group velocities and, hence, a different effective index of the individual guides. Therefore, employing a curvature allows for the optical simulation of a constant transverse electrical field $\Sigma(z)$. In the coupled mode regime, equation (15) reduces to

$$i\partial_z \varphi_m + c(\varphi_{m+1} + \varphi_{m-1}) = \omega \ddot{x}_0 m \varphi_m \quad (16)$$

for the amplitude φ_m in the m th waveguide, with $\omega = n_0 d / \lambda$ as a normalized frequency. The term $\omega \ddot{x}_0 m$ represents the transverse electrical field and can be tuned by an appropriate curvature of the waveguide array.

Optical Bloch oscillations

When the transverse field does not change with time, Felix Bloch showed that the evolving wavefunction exhibits an oscillatory motion in the lattice [29]. The optical analogue in a waveguide array would then require a parabolic curvature $x_0 \sim z^2$ of the array such that $\ddot{x}_0 = \text{const}$. The corresponding coupled mode equations then read [34]

$$i\partial_z \varphi_m + \alpha m \varphi_m + c(\varphi_{m+1} + \varphi_{m-1}) = 0, \quad (17)$$

where a constant transverse refractive index gradient αm with $\alpha = \omega \ddot{x}_0 = \text{const}$ is employed. In order to understand the dynamics of optical Bloch oscillations, it is instructive to begin with the evolution of a broad excitation with a Gaussian envelope and a flat phase. The respective Fourier transform $G(\beta_x d)$ is a narrow distribution and initially located around $\beta_x d = 0$. The evolution of this wave packet is depicted in figure 10 in reciprocal space (upper row) and real space (lower row). At the beginning of the Bloch cycle one obtains a vanishing transverse group velocity, which arises from the vanishing derivative of the band structure at $\beta_x d = 0$. However, the famous acceleration theorem [29] states that a constant gradient in real space yields a constant motion in Fourier space.

Hence, $G(\beta_x d)$ moves for $\alpha > 0$ with a constant velocity towards $+\beta_x d$ during the propagation, where the velocity is given by α/λ [35]. In this intuitive picture, $G(\beta_x d)$ follows the refractive index gradient, employing a transverse force in the $+\beta_x d$ -direction. As $G(\beta_x d)$ moves through the band structure without changing its shape, the spatial transverse profile of the beam remains in its shape as well. The transverse group velocity given by the derivative of the band determines the path of the beam propagation, which follows the band structure.

Following the propagation from $z = 0$ to $z = \pi/(2\alpha)$ corresponds to a motion in reciprocal space of $G(\beta_x d)$ from $\beta_x d = 0$ to $\beta_x d = \pi/2$, as shown in figure 10(a). At this point, the transverse group velocity reaches its maximum due to the maximal absolute value of the first derivative $\partial \beta_z / \partial \beta_x$ of the band structure (see figure 5(b)). Propagating further to $z = \pi/\alpha$, $G(\beta_x d)$ reaches $\beta_x d = \pi$ which is the edge of the Brillouin zone, where the transverse group velocity vanishes ($\partial \beta_z / \partial \beta_x = 0$). The occurring Bragg reflection on the periodic structure changes the transverse momentum, which corresponds to a transfer of $G(\beta_x d)$ to the other side of the Brillouin zone $\beta_x d = -\pi$ (see figure 10(b)). Note that, compared to the initial position, the beam experienced until now a transverse shift (which is proportional to the coupling coefficient c). Due to the symmetry of the band structure the propagation from $z = \pi/\alpha$ to $z = 2\pi/\alpha$ is similar to the first half period but with opposite sign of the transverse group velocity (see figure 10(c)). Hence, at $z = 2\pi/\alpha$ the beam reaches its initial position so the initial field distribution is restored and the periodic process is complete.

A different kind of geometric Bloch oscillations occurs for a narrow excitation, i.e. when only a single waveguide is excited. In this case light can no longer distinguish between left and right, since also the complex-conjugated wave packet φ_m^* is a solution of equation (17). Hence, the beam experiences a symmetric breathing and periodic refocusing.

Optical Bloch oscillations were first observed in waveguide lattices in 1999 by two groups [36, 37], by implementing a real transverse refractive index gradient in the lattice. The first experimental observation of Bloch oscillations in curved lattices was reported in 2004 [38], whereas Bloch oscillations in fs-laser-written waveguide

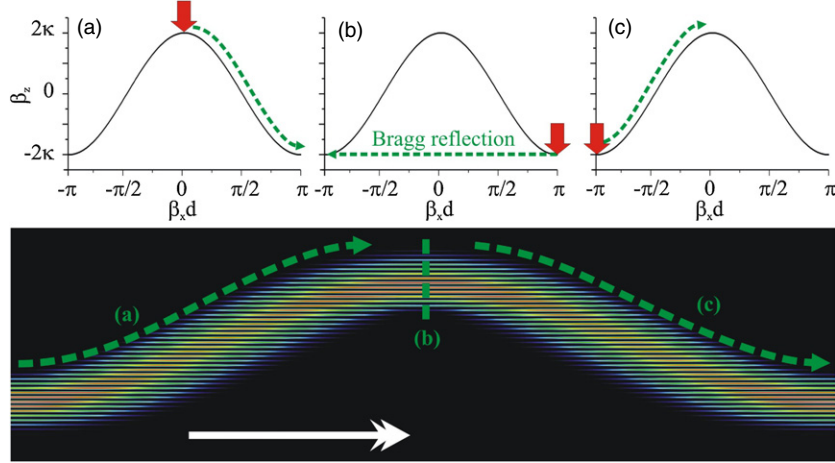


Figure 10. Optical Bloch oscillations. Upper row: motion of the spectral distribution G through the Brillouin zone. The red arrow marks the position of $G(\beta_x d)$. (a) $G(\beta_x d)$ moving from $\beta_x d = 0$ to the band edge. (b) Bragg reflection from $G(\beta_x d) = \pi$ to $G(\beta_x d) = -\pi$. (c) $G(\beta_x d)$ moving with constant velocity to the initial point $G(\beta_x d) = 0$. The lower row shows the corresponding propagation in real space (from left to right).

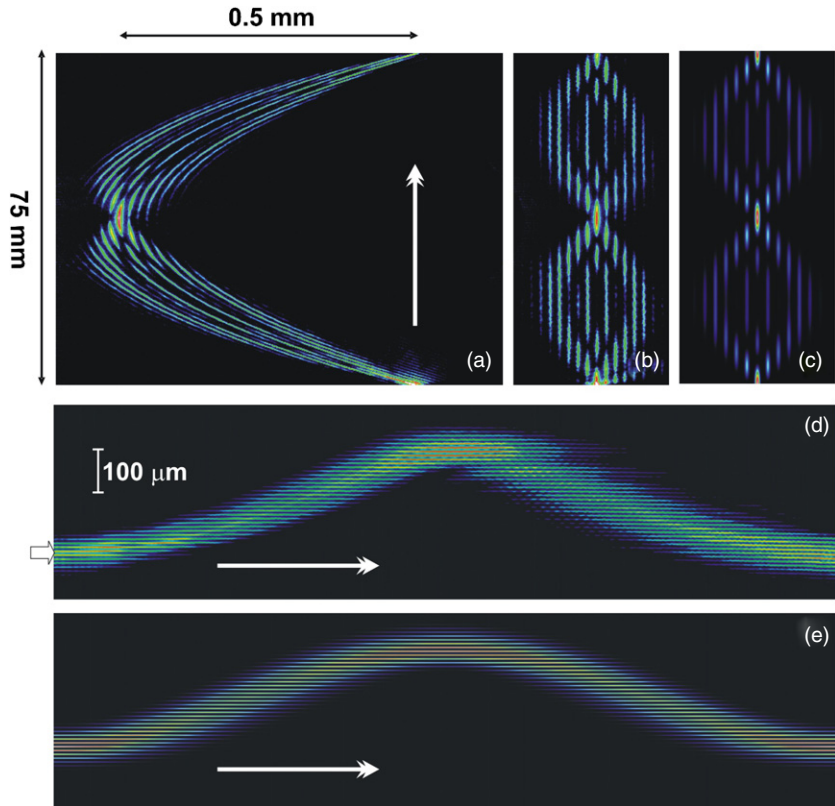


Figure 11. Fluorescence microscopy of optical Bloch oscillations. (a) In the original image the guides are circularly bent with a radius of $R = 1.21$ m, which causes a full lateral shift in the centre of the sample of $580 \mu\text{m}$. (b) In the digitally straightened image the image rows are shifted corresponding to the inverse bending profile, yielding an image in the curved coordinate system, in which the waveguides appear straight. (c) The corresponding simulations, solving equation (17) for a narrow excitation. (d) Bloch oscillations with a broad beam excitation. (e) The corresponding simulations, solving equation (17) for a broad beam excitation. Note that in (a)–(c) the propagation is from bottom to top, whereas in (d), (e) the propagation direction is from left to right. Figures from [40].

arrays were demonstrated for the first time in 2006 [39]. In a more general context, this experiment was repeated in 2009 [40]. The results are summarized in figure 11. The experiments were conducted in a 75 mm long sample. Applying a constant radius of curvature of $R = 1.21$ m yields

a full lateral shift of $580 \mu\text{m}$ (figure 11(a)). It is useful to perform a digital coordinate transform on this image by shifting every row by the respective negative bending profile $-x_0(z)$, resulting in the corresponding curvilinear coordinates where the waveguides appear straight. The light field broadens

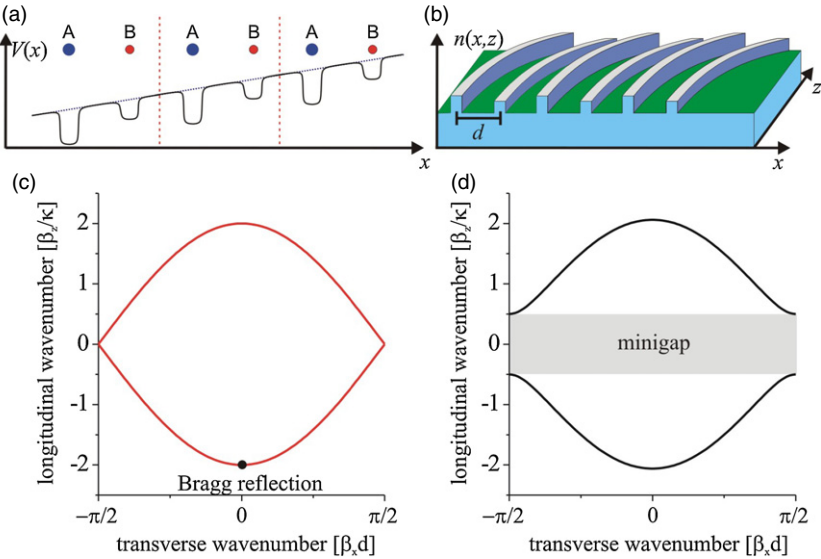


Figure 12. Setting for optical Bloch–Zener dynamics. (a) Sketch of a binary chain with a unit cell (marked by red dashed lines) consisting of two dissimilar atoms A (large blue) and B (small red). The corresponding potential has deep and shallow quantum wells and is superimposed by an external linear gradient (blue dotted line). (b) Sketch of the corresponding optical system. The unit cell consists of two waveguides with high and low effective indices and the linear external force is applied by a constant curvature. (c) Band structure (reduced to $|\beta_x d| \leq \pi/2$) of a homogeneous lattice. The point where Bragg reflection occurs is marked by a black dot. (d) Band structure of a binary superlattice with a detuning of $\sigma/c = 0.5$, showing two minibands which are separated by a minigap. Figures from [40].

and reaches a width of about 11 waveguides at a spacing of $14 \mu\text{m}$, before it relocates after every 37.5 mm of propagation (figure 11(b)). A simulation, where equation (17) was numerically integrated, is shown in figure 11(c). The situation for a broad excitation is depicted in figures 11(d) and (e). A radius of curvature of $R = 1.9 \text{ m}$ yields to an oscillation period of 75 mm. The centre of the beams experiences a shift of about 30 waveguides, according to the coupling strength at the lattice site spacing of $d = 11 \mu\text{m}$.

Optical Bloch–Zener dynamics

In recent experimental studies it was confirmed that Bloch oscillations come along with tunnelling to higher order bands [41], which is known as the Zener tunnelling [42]. But this process strongly dampens the Bloch oscillations and, more importantly, the larger width of higher propagation bands impeded the investigation of the interplay between Bloch oscillations and Zener tunnelling. However, using binary waveguide arrays this issue can be overcome. In these structures the individual bands split into minibands and interband tunnelling becomes possible. The benefit is that the Bloch oscillations are not damped which significantly simplifies the observation of Bloch–Zener dynamics [35].

The binary lattice has a unit cell, which contains two dissimilar sites. The corresponding potential consists of alternating deep and shallow wells (figure 12(a)), which arise from the two different sites. As the lattice period now is twice the one of the homogeneous array, the first band splits into two minibands separated by a minigap, which is determined by the different depths of the wells. In optics the corresponding potential is achieved by waveguides with alternating high and low refractive indices (figure 12(b)), which are expressed in

terms of a detuning σ to the average propagation constant of the system. The coupled mode equations then read

$$i\partial_z \varphi_m + (-1)^m \sigma \varphi_m + c(\varphi_{m+1} + \varphi_{m-1}) = 0. \quad (18)$$

The corresponding dispersion relation of the first band can be calculated as

$$\beta_z^\pm = \pm \sqrt{\sigma^2 + 4c^2 \cos^2 \beta_x d} \quad (19)$$

and is illustrated in figures 12(c) and (d), where figure 12(c) corresponds to the homogeneous lattice ($\sigma = 0$), whereas in figure 12(d) the detuning is set to $\sigma = c/2$. As predicted, the band splits into two minibands separated by a gap with a size $\sim \sigma$. Note that in the homogeneous array the Brillouin zone is $-\pi \leq \beta_x d \leq \pi$ (instead of $-\pi/2 \leq \beta_x d \leq \pi/2$ in the binary array), so for $\sigma = 0$ indeed equation (19) is equivalent to equation (7) and the two bands in figure 12(c) appear only due to the choice of the wrong limits.

As already described in the section about Bloch oscillations, the transverse gradient is employed by bending the waveguide array. When exciting the lattice with a broad Gaussian beam with a flat phase, the resulting initial narrow spectral distribution $G(\beta_x d)$ is centred around $\beta_x d = 0$ (figure 13(a)). Due to the acceleration theorem, $G(\beta_x d)$ moves towards the band edge $\beta_x d = \pi/2$ during the propagation. There, the presence of the minigap causes the wave to split into two parts. One part tunnels through the minigap (Zener-like tunnelling) to $\beta_x d = -\pi/2$ in the lower band, while the other part is Bragg reflected into the initial, upper miniband to $\beta_x d = -\pi/2$ (figure 13(b)). Propagating further results in a motion of $G(\beta_x d)$ from $\beta_x d = -\pi/2$ to the opposite band edge at $\beta_x d = +\pi/2$ in both minibands (figure 13(c)). Again, tunnelling and Bragg reflection occur; however, at this point the dynamics is much more complex due to the coherent combination of tunnelling and Bragg reflection. Since the

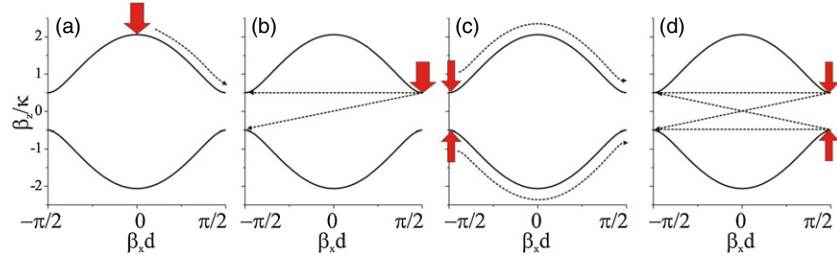


Figure 13. Tunnelling dynamics of one oscillation period. (a) Acceleration towards the band edge $\beta_x d = \pi/2$. (b) Bragg reflection in the upper band and tunnelling to the lower band. (c) Acceleration from $\beta_x d = -\pi/2$ to $\beta_x d = \pi/2$. (d) Second tunnelling process including overlay of Bragg reflection and tunnelling.

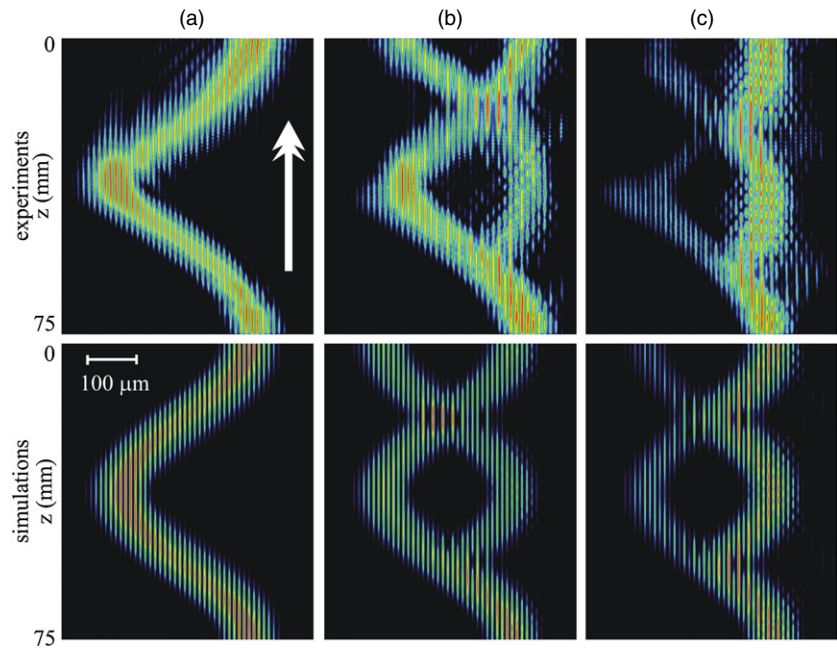


Figure 14. Fluorescence microscopy of Bloch–Zener dynamics with a broad beam excitation. (a) The homogeneous array shows complete tunnelling at every tunnelling point, resulting in conventional Bloch oscillations. (b) Slightly detuned array $\sigma/c = 0.22$ with a tunnelling rate of $\approx 65\%$ after the first tunnelling point. (c) Strongly detuned array $\sigma/c = 0.41$ with a low tunnelling rate of $\approx 25\%$. The propagation direction in all panels is bottom to up. Figures from [40].

lower miniband is now occupied, the Bragg reflected part of the wave packet in the upper band (from $\beta_x d = \pi/2$ to $\beta_x d = -\pi/2$) interferes with the fraction that tunnels from the lower band ($\beta_x d = \pi/2$) to the upper band ($\beta_x d = -\pi/2$), as shown in figure 13(d).

Bloch–Zener dynamics for three different situations are shown in figure 14, where in the upper row the experimental data [40] and in the lower row the simulations (equation (18)) are shown. The geometric parameters of $d = 11 \mu\text{m}$ and a radius of curvature $R = 1.90 \text{ m}$ yield an oscillations period of 75 mm, corresponding to the sample length. Figure 14(a) depicts the Bloch oscillations in a homogeneous array. In this case the gap between the bands vanishes, the Zener tunnelling rate is 100% and, hence, the excited upper band is fully occupied at the beginning and at the end of the sample, whereas the lower band has its maximum occupation at the sample’s centre. In figure 14(b), the array is detuned with $\sigma = 0.22 c$, corresponding to a tunnelling rate of 65%, which was achieved by lowering the writing velocity from 120 mm min^{-1} to 96 mm min^{-1} in every second waveguide.

As the size of the tunnelling regions is given by the width of $G(\beta_x d)$, a sufficiently broad beam experiences rapid tunnelling. One can clearly see how the beam spatially breaks up into two parts at the edge of the Brillouin zone, and then follows different paths due to the opposite curvature of the upper and the lower miniband. Further propagation results in refocusing of the light field at the edges of the Brillouin zone. Notably, the Zener tunnelling is much more complex at the second and later tunnelling points since light occupies both minibands and coherent interference determines the band occupancy after the crossings. Increasing the gap between the bands further to $\sigma = 0.41 c$ by reducing the writing velocity to 88 mm min^{-1} in every second waveguide decreases the tunnelling rate to $\sim 25\%$. Under these conditions, the initially excited band remains mostly occupied for the first Bloch period and only a small fraction of the light tunnels into the second miniband (figure 14(c)), effectively doubling the oscillation frequency compared to figure 14(a).

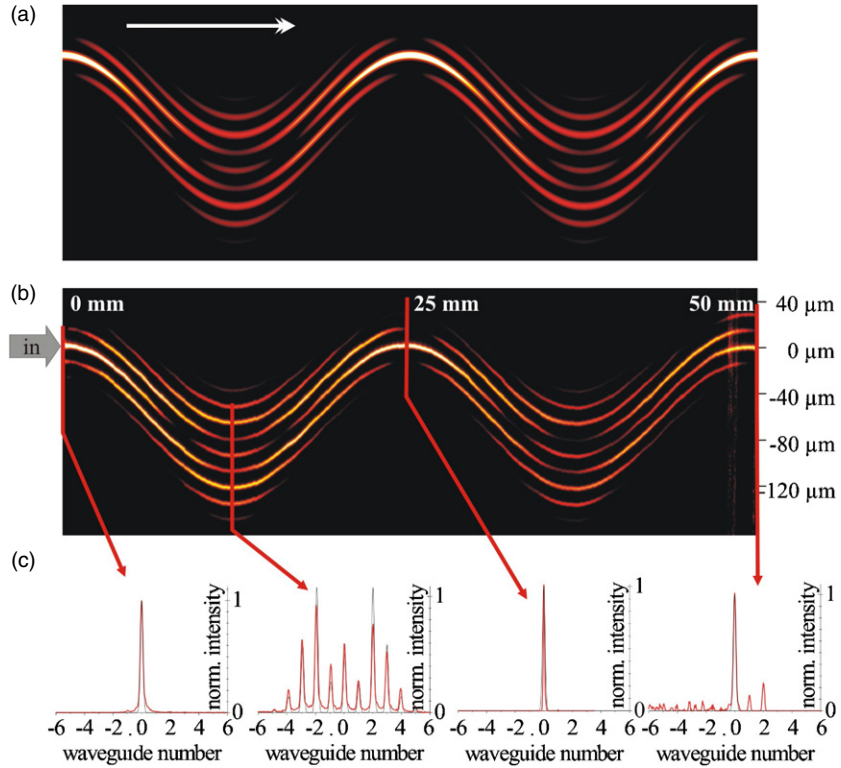


Figure 15. Fluorescence microscopy of optical DL in a 50 mm long sample. (a) Numerical simulation using equation (21), where the transverse Gaussian profile of the individual modes is digitally added to the waveguide intensities $|a_m|^2$. (b) Measured fluorescence image. (c) Measured (bold red) and simulated profiles (thin black) of the significant points (from left to right) $z = 0 \text{ mm}$, $z = 12.5 \text{ mm}$, $z = 25 \text{ mm}$ and $z = 50 \text{ mm}$. The propagation direction is from left to right. Figures from [25].

Dynamic localization

In contrast to Bloch oscillations, which occur in a constant linear transverse potential, it was predicted in 1986 that a transverse electric field, which is periodic in time (ac field), yields periodic collapse of the evolving wavefunction, which is well known as dynamic localization (DL) [43]. Although this periodic recovery is, at a first glance, very similar to Bloch oscillations, DL is based on fundamentally different mechanisms. Whereas for a constant transverse field the eigenvalues of the system are equally distributed [29, 34] yielding a periodic recovery of the initial field distribution, for a periodic ac field, the entire band collapses, preventing the wave packet from spreading over the lattice. However, the observation is difficult in most quantum systems as the required field strengths are too high. To overcome these limits, complex semiconductor superlattices with larger lattice periods have been used [30, 44, 45], although definitive evidence was still lacking [46]. Again, photonic structures provide the possibility of simulating such external potentials in curved waveguide arrays as well as of resolving the evolution dynamics [33, 47, 48].

In the optical analogue, the transverse ac field can be mimicked by a periodic bending of the waveguides

$$x_0 = A_0 \left(\cos \left\{ \frac{2\pi z}{z_0} \right\} - 1 \right) \quad (20)$$

so that the coupled-mode equations (16) reduce to

$$i\partial_z \varphi_m + c(\varphi_{m+1} + \varphi_{m-1}) = -\omega m A_0 \cos \left\{ \frac{2\pi z}{z_0} \right\} \varphi_m. \quad (21)$$

One can formally show [25, 33, 47] that after every full period $z \rightarrow z + z_0$, an effective coupling constant

$$c_{\text{eff}} = c J_0 \left(\frac{2\pi \omega A_0}{z_0} \right) \quad (22)$$

can be defined, with $J_0(x)$ as the zeroth Bessel function of the first kind. Evidently, at z_0 the effective coupling vanishes for the resonance condition

$$\frac{\omega A_0}{z_0} = \frac{n_0 d A_0}{\lambda z_0} = \eta_j, \quad (23)$$

where η_j is the j th root of the equation $J_0(\eta_i) = 0$ (i.e. $\eta_1 = 2.405$, $\eta_2 = 5.520, \dots$). Hence, for a fixed waveguide spacing d and a wavelength λ , DL is obtained only for the particular ratios A_0/z_0 and the wave packet collapses at z_0 . This is in strong contrast to Bloch oscillations, which are obtained for every transverse constant field.

The experimental realization of DL in fs-laser-written waveguide arrays is presented in figure 15. In figure 15(a), the numerical integration of equation (21) is shown, figure 15(b) shows the experimentally obtained data using fluorescence microscopy and figure 15(c) depicts the cross sections of the light field at different positions. For a sample length of 50 mm, a waveguide spacing of 14 μm and a chosen period of $z_0 = 25 \text{ mm}$, a bending amplitude of $A_0 = 47.5 \mu\text{m}$

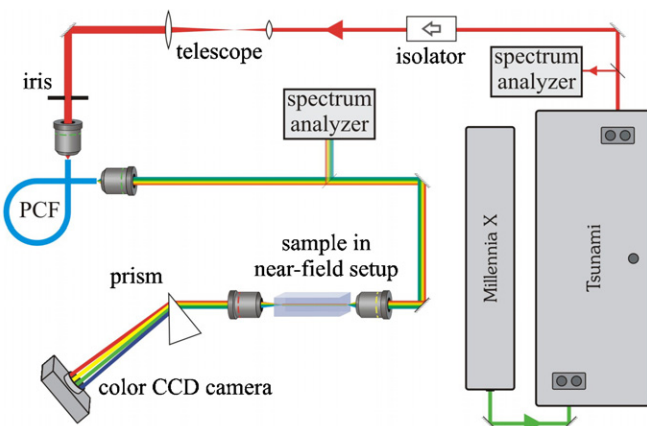


Figure 16. Setup for observing a spectrally resolved output pattern. An optical supercontinuum is generated by the propagation of an ultrashort pulse through a highly nonlinear fiber (PCF). The white light is spectrally and spatially resolved after propagation through the waveguide array using a prism for dispersion and projection onto a CCD camera. Figures from [25].

follows from equation (23) for a wavelength of $\lambda = 633$ nm. Initially, a single waveguide is excited. After a propagation distance of 12.5 mm the light field spreads across about nine waveguides before it starts to relocalize in order to collapse after 25 mm. However, DL is only exact for coupling restricted to the immediate neighbours. Since the investigated systems feature slight higher-order coupling to sites beyond direct neighbours with a relative strength of 3% and also contain small imperfections inside the array, no perfect refocusing of the excitation is obtained. This is even more pronounced after two periods, where imperfections and coupling effects have accumulated. It is important to understand that in most cases the impact of next-nearest neighbour coupling can be safely neglected since the deviations from pure nearest-neighbour coupling is only marginal; however, when this first order is suppressed as for DL, any higher-order coupling becomes visible. A discussion of higher-order coupling can be found in [49], whereas an experimental analysis is reported in [50].

The resonant behaviour of DL can also be analysed with respect to the excitation wavelength. For this purpose an optical supercontinuum is generated by injecting fs pulses into a highly nonlinear fibre, resulting in spectral broadening up to an almost octave spanning spectrum in the visible range. A camera records the near-field output pattern after dispersive splitting induced by a prism, as shown in figure 16. Figure 17 illustrates the self-imaging property in the output spectrum for two samples designed for different wavelengths. The waveguide spacing is fixed to $d = 16 \mu\text{m}$ and the bending period of 25 mm is equal to the sample length. The respective curving amplitudes are $A_0 = 36 \mu\text{m}$ for $\lambda = 543 \text{ nm}$ (figure 17(a)) and $A_0 = 42 \mu\text{m}$ for $\lambda = 633 \text{ nm}$ (figure 17(b)). In both images it is clearly shown that DL occurs for the design wavelengths solely, whereas for other wavelengths in the vicinity of the design wavelengths the localization is incomplete.

Polychromatic dynamic localization

Integrated optical devices based on self-imaging provide a variety of attractive applications, including image transmission, optical collimation or even reshaping of ultrashort laser pulses [51–53]. Image reconstruction, first considered in slab waveguides [54], was for example shown in homogeneous waveguide arrays due to the discrete analogue of the Talbot effect, yielding periodic self-imaging for certain initial field distributions [55]. More general types of periodic input recovery can be realized by using optical BO or optical DL in properly engineered lattices. The main drawback of these mechanisms is the rather small bandwidth of operation. In the case of DL, the destruction of self-imaging for broadband beams stems from the resonant nature of equation (23), whereas for BO the self-imaging period turns out to be proportional to the wavelength λ . However, in order to render waveguide arrays interesting for applications, an increase in the bandwidth is highly desirable in order to achieve broadband operation.

Here, we present a generalized DL, in which the stringent resonant condition (23) is softened in order to achieve an approximated DL over an extremely broad spectral region. The basic idea relies on the fact that equation (23) has infinite solutions as sketched in figure 18(a) [56]. However, in the vicinity of the resonances at η_j the sign of the effective coupling alternates. For example, for the design wavelength $\lambda = 550 \text{ nm}$ at the first two resonances one finds $c_{\text{eff}}(\lambda_1 - \varepsilon) < 0$ and $c_{\text{eff}}(\lambda_2 - \varepsilon) > 0$, as shown in figure 18(b) (note the optical frequency ω , i.e. $1/\lambda$ is plotted). A combination of both resonances would therefore yield a strongly reduced effective coupling, which effectively vanishes over a broad spectral region (see the red curve in figure 18(b)). Therefore, a sample was fabricated which exhibits a bending consisting of two segments where the first segment meets condition (23) for $\eta_1 = 2.405$ (first-order DL) and the second one for $\eta_2 = 5.520$ (second-order DL). The resulting profile is sketched in figure 18(c). For a waveguide spacing of $d = 26 \mu\text{m}$ and a design wavelength of $\lambda = 550 \text{ nm}$, following the analysis in [56] yields for the first section $A_1 = 56 \mu\text{m}$ and $z_1 = 63 \text{ mm}$, and for the second section $A_2 = 86 \mu\text{m}$ and $z_2 = 42 \text{ mm}$. The experiments demonstrate that with such a device DL is achieved over the entire visible spectral region from 450 nm to 700 nm. Figure 18(d) shows the propagation in the sample at $\lambda = 633 \text{ nm}$, whereas in figure 18(e) the spectrally resolved output pattern is shown [57]. In comparison, in figure 18(f) the spectrally resolved output pattern for the straight lattice is shown, exhibiting strong diffraction for all spectral components.

Notably, polychromatic DL, together with recently proposed polychromatic Bloch oscillations [58], opens up new avenues for applications in various physical contexts. In particular, these results suggest new approaches for flexible shaping of polychromatic light with ultrabroadband or supercontinuum spectra, which can be enhanced further through the introduction of structure tunability and optical nonlinearities.

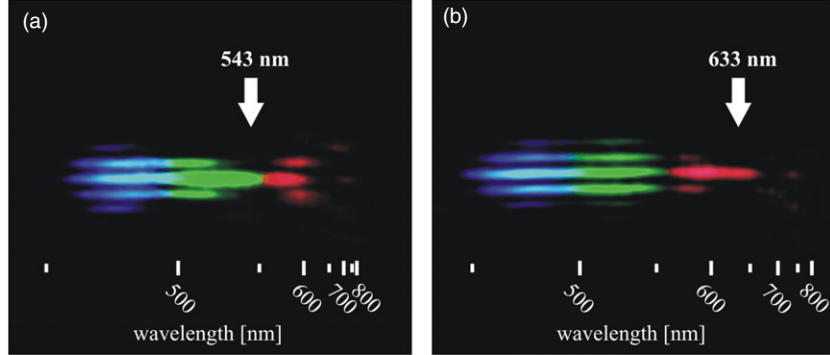


Figure 17. Spectral characterization of DL. (a) End facet of a curved waveguide array, designed for DL at $\lambda = 543$ nm analysed using the setup in figure 16. (b) A similar sample, designed for $\lambda = 633$ nm. Figures from [25].

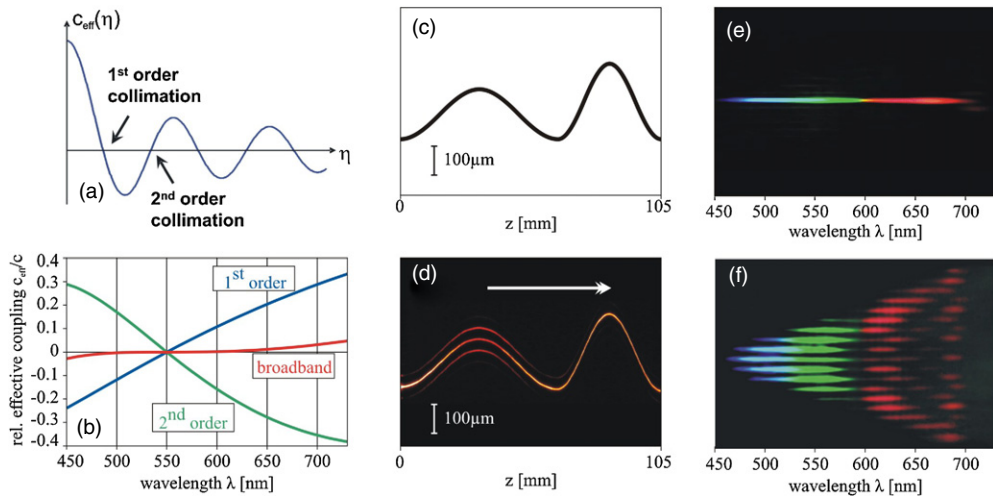


Figure 18. Realization of broadband DL. (a) Since $c_{\text{eff}} \sim J_0(\eta) = 0$ has an infinite number of roots, not only first order DL ($\eta_1 = 2.405$), but also higher order DL (e.g. $\eta_2 = 5.520$) is possible. (b) Theoretical effective coupling for first (dashed blue) and second (dotted green) order DL and their combination (solid red). (c) Sketch of the curvature of the waveguide array for broadband coupling. The design (central) wavelength is 550 nm. (d) Fluorescence microscopy of the light propagation at $\lambda = 633$ nm. The propagation direction is from left to right. (e) Spectrally resolved output pattern in the visible spectral region. (f) Comparison to the output of a straight array. Figures from [55].

Self-imaging in waveguide arrays by segmentation

The self-imaging methods presented so far rely on boundary-free propagation; truncated array structures lead to considerable distortions of the self-imaging effect. This can be overcome by a particular modification of the coupling constants [59]; however, the extreme precision required does not seem viable with current fabrication techniques.

Recently, it was suggested that introducing specific phase shifts to the propagating modes by a segmentation of the waveguide arrays can yield image reconstruction for arbitrary 1D and 2D intensity distributions even in finite configurations involving boundary reflections [60]. In order to explain the idea, first a finite planar (1D) array $i\partial_z\varphi_m = -c(\varphi_{m+1} + \varphi_{m-1})$ is considered with waveguides $m = 1, \dots, M$. One can show [55] that this equation is fulfilled by a set of M propagation invariant orthonormal supermodes $\varphi_m^k = a_m^k \exp\{-i\beta_k z\}$ with the shape

$$a_m^k = \sqrt{\frac{2}{M+1}} \sin\left\{\frac{mk\pi}{M+1}\right\} \quad (24)$$

(see figure 19 for an array with $M = 9$ waveguides) and the corresponding propagation constant

$$\beta^k = -2c \cos\left\{\frac{k\pi}{M+1}\right\} \quad (25)$$

of the k th supermode ($k = 1, \dots, M$). One can easily show that introducing a phase shift of π in every second waveguide results in a pairwise conversion of the individual supermodes, as shown exemplarily in figure 20(a) for the mode a_m^1 , which is transformed into a_m^9 . Importantly, different supermodes exhibit different propagation constants (equation (25)). Hence, assuming a sample of length L and introducing the phase shift at position $L/2$, the diffraction occurring in the region $z < L/2$ is reversed in the region $z > L/2$, so the initial intensity distribution $|\varphi(0)|^2$ is imaged on the output facet $|\varphi(0)|^2 = |\varphi(z)|^2$. This is schematically shown in figure 20(b). A genuine way of impressing such a phase shift on the propagating modes is the alternating segmentation of the waveguides, so the accumulated additional phase shift in the

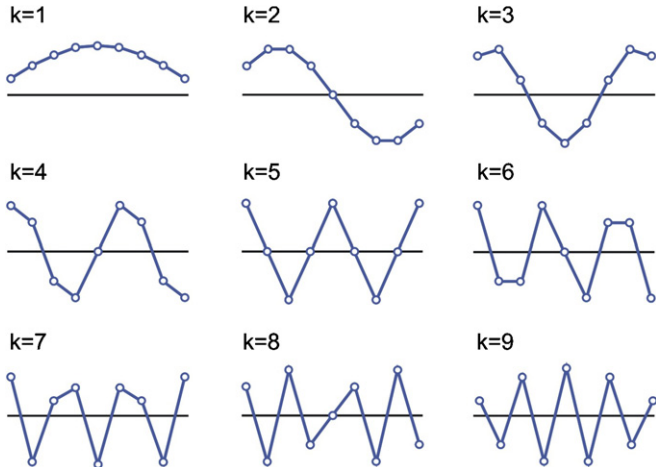


Figure 19. The amplitude distributions (equation (24)) of the supermodes in a planar waveguide array with $N = 9$ waveguides.

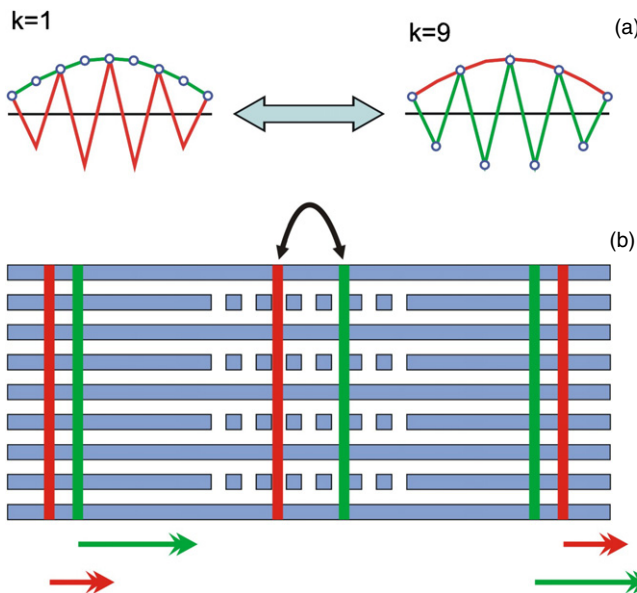


Figure 20. Impact of the segmentation. (a) Transformation of the first supermode into the ninth supermode and vice versa by a phase flip of π in every second waveguide. (b) Due to the mode transformation in the sample centre by the phase flip and the different velocities of the supermodes, the superposition of the supermode at the input is resembled at the output facet.

propagating modes with the wavelength λ in every second waveguide is

$$\Delta\phi = \frac{2\pi s}{\lambda} (n_{\text{eff}} - n'_{\text{eff}}) = \pi, \quad (26)$$

where s is the length of the segmentation and n_{eff} and n'_{eff} are the effective refractive indices of the unsegmented and the segmented waveguides (in the segmented region), respectively. A sketch of this setting is shown in figures 21(a) and (c) for a 1D array and a 2D array, respectively.

Using the fs laser writing technique, a segmentation can be simply realized by switching a shutter periodically on/off during the writing process [61]. A 1D sample with length $L = 50$ mm and a waveguide spacing of $d = 16 \mu\text{m}$ was designed

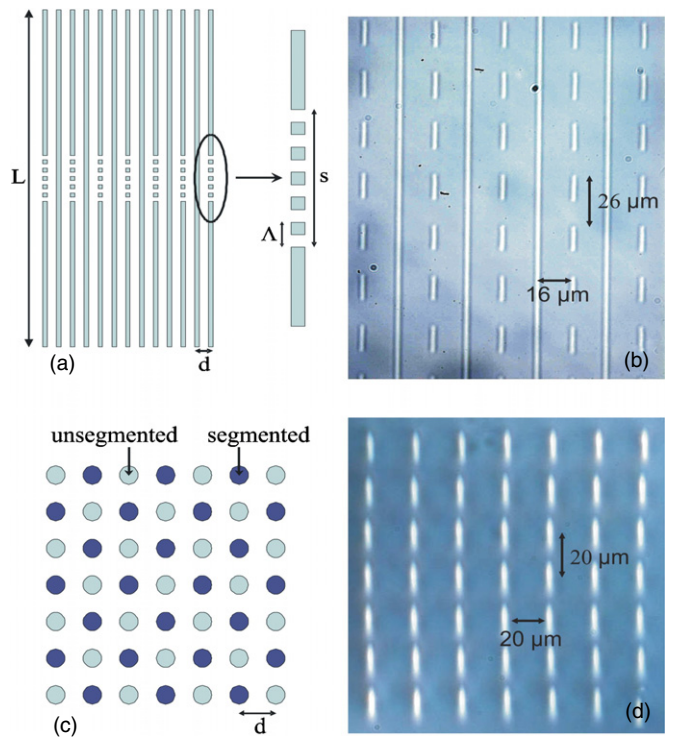


Figure 21. Fabricated samples for the self-imaging. (a) Sketch of the 1D array configuration. (b) Microscope image of the segmented region. (c) Sketch of the 2D array configuration. (d) Microscope image of the front facet of the fabricated square lattice. Figures from [59].

for perfect imaging at $\lambda = 633 \text{ nm}$. For a segmentation period of $\Lambda = 26 \mu\text{m}$ the required length of the segmented region is $s = 2.6 \text{ mm}$, according to the fabrication parameters used for these waveguides (for a sketch of the 1D configuration see figure 21(a)). The respective micrograph of the segmented region is shown in figure 21(b). In the unsegmented array, light at a wavelength of $\lambda = 633 \text{ nm}$ experiences strong diffraction and spreads across the array, as shown in the fluorescence images (figures 22(a) and (b)) for central and edge waveguide excitations. However, this behaviour is significantly altered by the segmentation. As soon as the light encounters the phase shift, diffraction reverses and the initial light distribution is restored. This effect is independent of the presence of array boundaries, as can be observed for central as well as edge excitation (see figures 22(c) and (d)). Obviously, the segmented region is sufficiently small compared to the coupling length $l_c = \pi/2c \approx 15 \text{ mm}$ to satisfy the condition of an abrupt phase shift with reasonable accuracy, as is confirmed by the agreement with the respective simulations (figures 22(e) and (f)). As more complex intensity distributions are simply a superposition of a set of single waveguide excitations, this setting therefore allows for the imaging of arbitrary input signals. The resolution of the image is only restricted by the number of waveguides in the array.

The concept of phase shift-induced image reconstruction can be extended to the 2D square lattice, since it can be described by the superposition of horizontal and vertical 1D lattices as long as the impact of coupling between waveguides along the diagonal is negligible. A sketch of

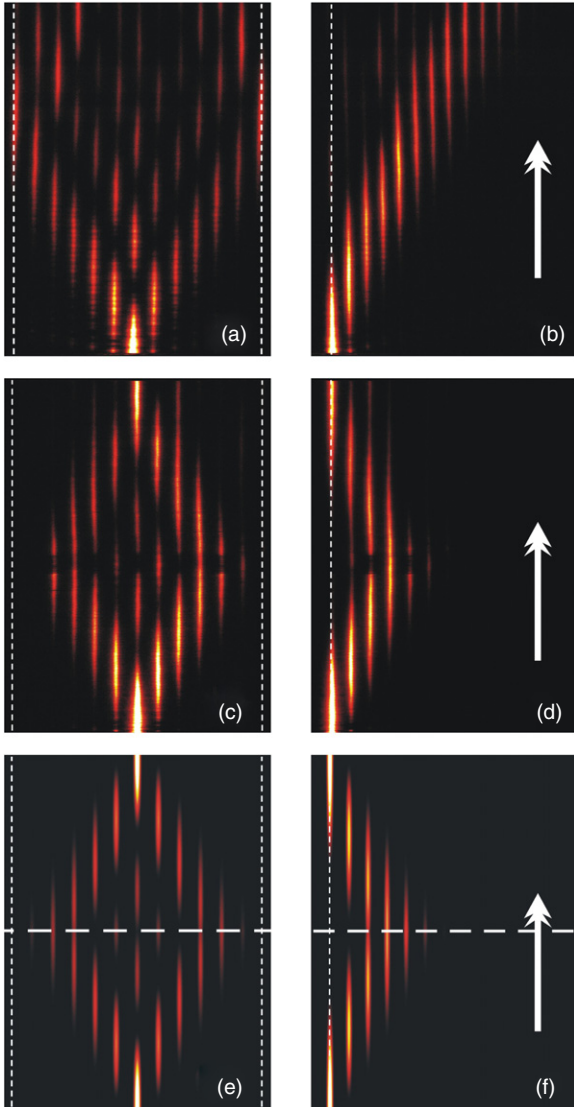


Figure 22. 1D imaging by segmentation. (a), (b) Light evolution in an unsegmented array for centre and edge waveguide excitations. (c), (d) A segmentation causes an inversion of the diffraction so the input plane is imaged onto the output facet regardless of centre or edge waveguide excitation. (e), (f) The simulations support the assumption of an abrupt phase shift, which is marked with a horizontal dashed line. The propagation direction in all panels is from bottom to top. Figures from [59].

the two-dimensional arrangement is depicted in figure 21(c); a micrograph of the array front facet is shown in figure 21(d). In this case a spacing of $d = 20 \mu\text{m}$ was chosen together with $\Lambda = 26 \mu\text{m}$ and $s = 2.6 \text{ mm}$ as period and length of the segmentation, respectively. The observed diffraction patterns in the unsegmented array for two different excitation sites are shown in figures 23(a) and (b). In both cases, light spreads across a significant part of the array. The associated simulated distributions are shown in figures 23(c) and (d). Under the influence of segmentation, the light has returned to the respective excited waveguides when it reaches the end facet, as shown in figures 23(e) and (f).

Since this novel method is independent of array boundaries, it therefore provides a versatile method for exact

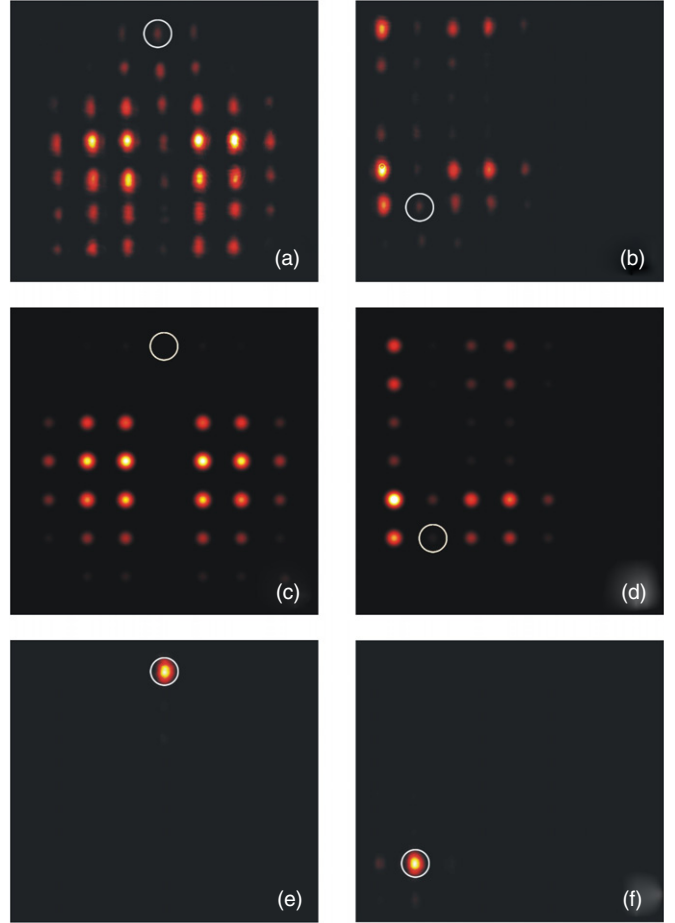


Figure 23. 2D imaging by segmentation. (a), (b) The light distribution at the output facet of a 2D 7×7 lattice without segmentation for two different excitations. (c), (d) The corresponding simulations. (e), (f) The output distribution in the respective segmented arrays. The excited waveguides are marked with a white circle. Figures from [59].

image transmission in a variety of configurations in integrated optics. The experiments were carried out with a quasi-monochromatic continuous-wave helium–neon laser as an excitation source; however, preliminary numerical simulations have revealed that this imaging method is also applicable to large bandwidth signals and accordingly for short pulses as well.

Nonlinear discrete optics

Many physical systems that behave linearly for small input powers become nonlinear as the input power increases. However, nonlinearity is often ignored in the analysis of many systems due to unwanted complexity. Unfortunately, the principle of superposition breaks, i.e. the independent propagation of the individual optical fields. This is the reason why a linear dependence is assumed as often as possible to describe physical systems. Nevertheless, nonlinear phenomena reveal various new and interesting aspects of physics. Many of the developments of today’s networked world rely on nonlinearity such as the high-speed optical

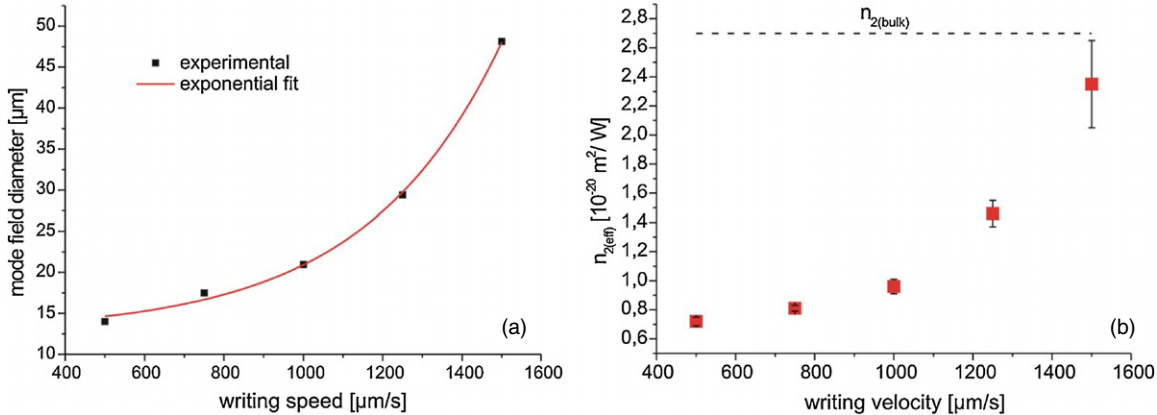


Figure 24. Impact of the fabrication parameters on the nonlinear properties of fused silica. (a) Dependence of the modal $1/e^2$ -width d_{mode} at $\lambda = 800 \text{ nm}$ on the writing velocity for the fabrication parameter of 150 fs pulse duration and $0.3 \mu\text{J}$ pulse energy. (b) Dependence of the effective nonlinear refractive index $n_{2(\text{eff})}$ on the writing velocity. Figures from [23].

communication links that provide the infrastructure for today's voice and data networks, optical storage for consumer devices and computers along with a whole array of medical and biotechnological advances.

The study of discrete nonlinear phenomena goes back to 1939, when plastic deformations of crystals were investigated in detail [62]. However, it took almost 40 years before the concept of a discrete spatial soliton was introduced for the description of nonlinear energy localization in protein molecules [63]. Then, in 1982, an analytical solution of two nonlinear coupled harmonic oscillators was found [64], describing a system of two evanescently coupled nonlinear waveguides. The first relation between nonlinear localization and arrays of evanescently coupled waveguides was established in 1988, when it was predicted that in one-dimensional lattices light can be trapped in only a few waveguides by the influence of a $\chi^{(3)}$ nonlinearity [65]. Hence, for a sufficiently high input power the linear diffraction of the light can be counterbalanced by the nonlinearity, so-called discrete spatial solitons can exist in waveguide lattices, which was experimentally verified in planar ridge waveguide arrays etched into an AlGaAs substrate [66]. Since waveguide arrays, where the discrete nature of the system breaks the spatial symmetry, support a variety of nonlinear states which are unstable and cannot be observed in continuous media, these systems provide not only the basis for new fundamental research but also for various innovative applications such as all-optical routing, switching and storage devices [5, 67].

Reduced nonlinear refractive index

For a 1D array, the nonlinear generalization of equation (4) reads

$$i \frac{\partial}{\partial z} \varphi_m + c (\varphi_{m-1} + \varphi_{m+1}) + \gamma |\varphi_m|^2 \varphi_m = 0 \quad (27)$$

with the nonlinear coefficient

$$\gamma = n_{2(\text{eff})} \frac{n_0 \varepsilon_0 \omega}{2 A_{\text{eff}}} \quad (28)$$

Here, $\omega = 2\pi/\lambda$ is the angular frequency, ε_0 is the dielectric constant and n_0 is the refractive index of the bulk material. The

quantity $n_{2(\text{eff})}$ is a function of the $\chi^{(3)}$ nonlinearity and known as effective nonlinear refractive index, whereas A_{eff} is the effective area of the guided mode in the individual waveguides and can be approximated by $A_{\text{eff}} \approx \pi r^2$ with r as the $1/e^2$ -width of the mode. For increasing writing velocities during the fabrication process the refractive index change becomes smaller (see figure 7(b)) causing a weaker guiding and, hence, a weaker confinement which results in an increase of r . For an excitation wavelength of $\lambda = 800 \text{ nm}$ this is depicted in figure 24(a). However, since during the writing process the molecular structure of the bulk material is modified, also the nonlinear refractive index is a function of the writing velocity, as summarized in figure 24(b). Interestingly, while for high writing speeds the nonlinearity is almost not affected and reaches the value for the unprocessed bulk material ($n_{2(\text{bulk})} = 2.7 \times 10^{-20} \text{ m}^2/\text{W}$ at $\lambda = 800 \text{ nm}$ [68]), with decreasing velocity also the effective nonlinear refractive index drops to only $n_{2(\text{eff})} = 0.25n_{2(\text{bulk})}$ [23, 69]. Thus, the effective nonlinearity can be specifically tuned in order to tailor the nonlinear propagation properties.

1D discrete solitons

Although the formation of a one-dimensional discrete soliton seems to be similar to a nonlinear Kerr lens, which focuses the travelling high-intensity beam [70, 71], the underlying mechanisms differ. The additional phase shift induced by the nonlinear term $\gamma |\varphi_m|^2 \varphi_m$ in equation (27) moves the propagation constant of the excited guide into the semi-infinite gap above the first band as shown in figure 25(a). Hence, this guide cannot 'communicate' with the rest of the array, so it forms an isolated state and the light remains 'trapped'. The width of the band in the 1D case can be obtained from equation (7) to $\Delta\beta_z = (\beta_z^{(\text{max})} - \beta_z^{(\text{min})}) = 2c$. Since the nonlinear contribution to the propagation constant is $\delta\beta_z^{(\text{nonl})} = \gamma |\varphi_m|^2$ according to equation (27), the critical power for soliton formation can be roughly estimated by $|\varphi_m|_{\text{crit}}^2 = 2c/\gamma$. It is important to note that in fused silica γ is positive; therefore, the nonlinear contribution is also positive. In some materials, under particular conditions, γ may

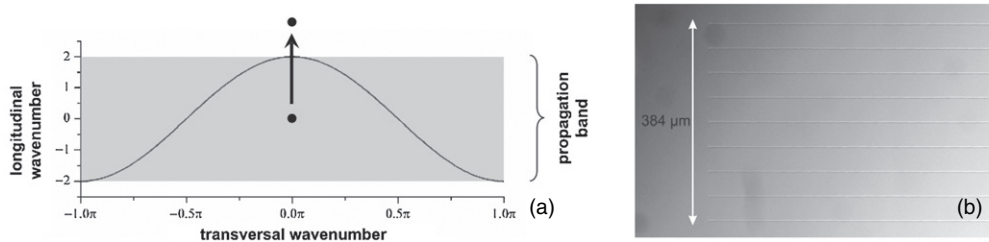


Figure 25. Fundamentals for the excitation of discrete solitons. (a) When exciting a waveguide with a high-power beam, the nonlinearity (see equation (27)) causes an additional contribution to the propagation constant $\delta\beta_z^{(\text{nonl})}$, therefore shifting β_z out of the band, so that the waveguide cannot ‘communicate’ with the surrounding guides and forms an isolated (nonlinear) state. (b) Microscope image of a planar waveguide array, consisting of nine waveguides with a separation of $48 \mu\text{m}$.

be negative, so the propagation constant can be decreased until it reaches the finite gap between the first and the second band, resulting in the formation of discrete gap solitons [72].

When writing the waveguides into fused-silica samples, the electronic $\chi^{(3)}$ nonlinearity provides an almost instantaneous response of the system, but is rather weak. Therefore, a high input peak power is required for the excitation of discrete solitons in these lattices, so that the experimental analysis relies on powerful laser sources. Hence, for the demonstration of the nonlinear discrete self-focusing a pulsed fs laser beam may be used, which provides the required peak power. In our experiments, we used a Ti:sapphire laser system (Spitfire, Spectra-Physics) with a pulse duration of about 150 fs, a repetition rate of 1 kHz and pulse energies of up to $3 \mu\text{J}$ at 800 nm. The light was coupled into the centre waveguide with a $4\times$ microscope objective ($\text{NA} = 0.10$), coupled out by a $10\times$ objective ($\text{NA} = 0.25$) and projected onto a CCD camera. The relatively low focusing of the incoupling objective ensured that pulses with a higher peak power could be launched into the array before the damage threshold of the sample was reached. The power of the beam was measured before the incoupling and after the outcoupling objective using a beam splitter. Using this setup, the power coupled into the waveguides was calculated considering Fresnel losses, damping and the overlap integral of the focal spot of the incoupling microscope objective and the shape of the propagating mode in every waveguide. For the first demonstration of a 1D discrete soliton in a fs-written array, a planar 74.5 mm long sample consisting of nine waveguides with a separation of $48 \mu\text{m}$ was fabricated at a writing velocity of $500 \mu\text{m s}^{-1}$. A microscope image of the sample is shown in figure 25(b). The experimental difficulties arise from balancing linear coupling which is desirably strong, input peak power which is high enough to achieve localization without breaking the sample and a propagation length which allows considerable diffraction without having the intrinsic waveguide losses (approximately 0.4 dB cm^{-1} in our experiments) to overcome the nonlinear propagation. Even such low losses accumulate to significant values after some centimetres of propagation. The maximum peak power of the incoupled pulses is limited by the damage threshold of the sample. Therefore, the waveguides are buried 0.5 mm away from the incoupling facet, since the sample surface has a significantly lower damage threshold than the bulk material. This reduces the applied fluence at the sample surface and

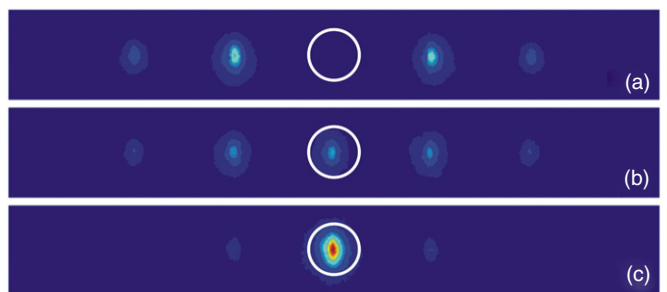


Figure 26. Formation of a 1D discrete soliton in the experiment. (a) Linear diffraction pattern at the sample output. (b) Intermediate localization for $P_{\text{peak}} = 500 \text{ kW}$ input peak power. (c) Almost complete light trapping in the excited waveguide for $P_{\text{peak}} = 1000 \text{ kW}$. The sample was 74.5 mm long, the waveguide spacing was $48 \mu\text{m}$ and the fabrication was performed at $3 \mu\text{J}$ pulse energy and $500 \mu\text{m s}^{-1}$ writing speed. The excited waveguides are marked with a white circle. Figures from [71].

allows to couple pulses at a substantially higher peak power into the waveguides. The measured intensity distribution at the sample output is depicted for three different peak powers launched into the central guide in figure 26(a)–(c). Whereas in the lower peak power range almost all of the guided energy is coupled to the adjacent waveguides due to linear coupling, at $P_{\text{peak}} = 500 \text{ kW}$ input peak power the pattern already shows some light which is trapped in the excited guide. Eventually, at a peak power of $P_{\text{peak}} = 1000 \text{ kW}$ the output intensity pattern is almost completely localized [73]. It is important to note that there is always some linear background in the non-excited guides and localization will never be perfect due to the excitation with pulsed light. Whereas the high power is sufficient for localization in the central part of the pulse, the pulse wings still experience linear diffraction due to their significantly lower power. A comparison of the experimental data with simulation is shown in figure 27, which still exhibits an excellent agreement in the dependence of the amplitudes in the individual waveguides. Clearly, the collapse of the diffraction is seen when the propagation constant of the excited guide leaves the band and moves into the gap. It is important to note that for the numerical modelling a reduced nonlinear coefficient γ using $n_2(\text{eff}) = 0.25n_2(\text{bulk})$ was used, which is consistent with figure 24(b) since the array was fabricated with a writing velocity of $500 \mu\text{m s}^{-1}$.

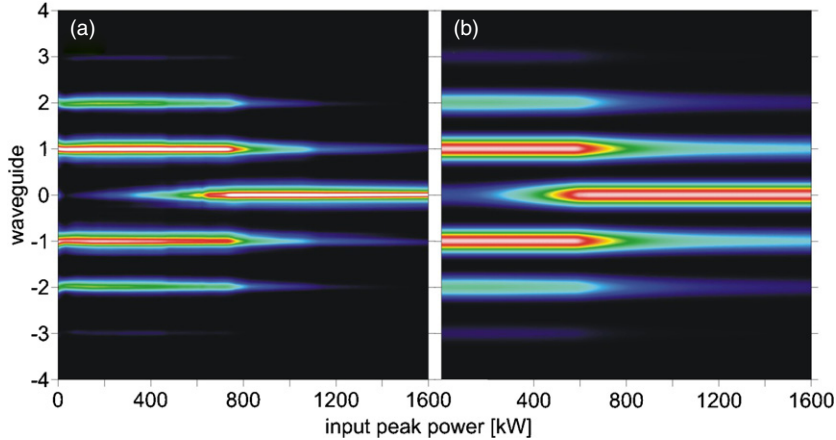


Figure 27. Comparison between experiment and theory. The amplitude in the n th waveguide is shown as a function of the input power. (a) The experimental data, showing the collapse of the diffraction pattern around $P_{\text{peak}} = 800$ kW. (b) The numerical analysis, assuming a reduced refractive index according to figure 24(b). Figures from [71].

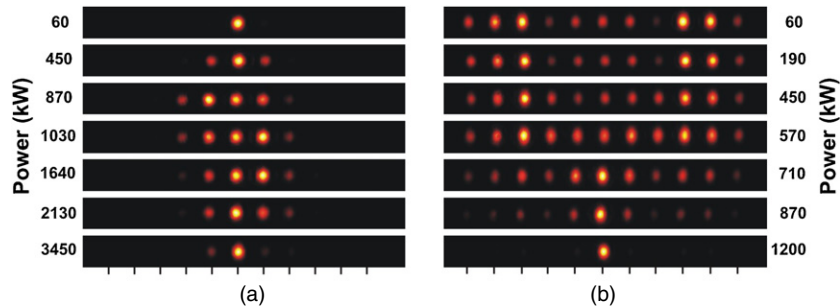


Figure 28. Formation of diffraction-managed solitons in the experiment. (a) Different output patterns for different input powers in a periodically curved waveguide array. The suppression of the linear diffraction due to DL is overcome by the nonlinearity, so the beam spreads. Only at sufficiently high power the beam localizes and forms a soliton. (b) Output patterns in a straight array as a function of the input power. The threshold for soliton formation in this lattice is well below the threshold in the curved lattice. (a), (b) The central waveguide was excited.

One can clearly see that the nonlinear propagation in waveguide lattices is much more complex than simple Kerr lensing when one analyses the nonlinear light propagation in periodically curved lattices. As described in the previous section, a bending which fulfils equation (23) results in DL, i.e. the localization of light after each full bending period, in the low-power regime. However, increasing the input peak power affects the sensitive phase relation between the adjacent guides due to the induced nonlinear change of the refractive index in the guides, resulting in delocalization of the output pattern, although the nonlinearity is focusing. This phenomenon is known as nonlinear diffusion [74]. In this setting, solitons form only for much higher peak power compared to their counterparts in straight lattices due to the altered phase relation between adjacent guides which is caused by the bending. In figure 28, the experimental verification of this phenomenon is demonstrated [75]. In figure 28(a), the evolution of the output pattern as a function of the input peak power is shown for a 105 mm long sample with a waveguide spacing of $d = 34 \mu\text{m}$. The localization period was chosen to be equal to the sample length (i.e. $z_0 = 105 \text{ mm}$) and the required bending amplitude was $A = 104 \mu\text{m}$. For $P_{\text{peak}} = 70 \text{ kW}$ launched into a single waveguide light dynamically localizes

in the excited channel at the output facet. When the peak power is increased to $P_{\text{peak}} = 1030 \text{ kW}$, the light spreads significantly since the phase relation between adjacent guides is changed so that DL is no longer observed. Importantly, the output pattern is asymmetric according to the asymmetric sample (compare figure 15). Eventually, at $P_{\text{peak}} = 3450 \text{ kW}$ the nonlinear focusing overcomes the spreading and a discrete soliton forms. However, the required power for soliton formation is much higher than in the straight lattice, where localization takes place already at $P_{\text{peak}} = 1200 \text{ kW}$ (see figure 28(b) for a straight sample exhibiting the same parameters as in figure 28(a), except $A = 0 \mu\text{m}$).

2D discrete solitons

It was demonstrated by Kelley [76] that 2D solitons in homogeneous media are unstable, i.e. they exist only at the critical power. For lower power, the beam still spreads, and for higher power the beam collapses. However, one can show that the shallow refractive index variations of a waveguide array support the stability of 2D solitons [3]. Hence, 2D discrete solitons exhibit unusual features, with no counterpart in the continuous regime [5]. The first experimental observation of

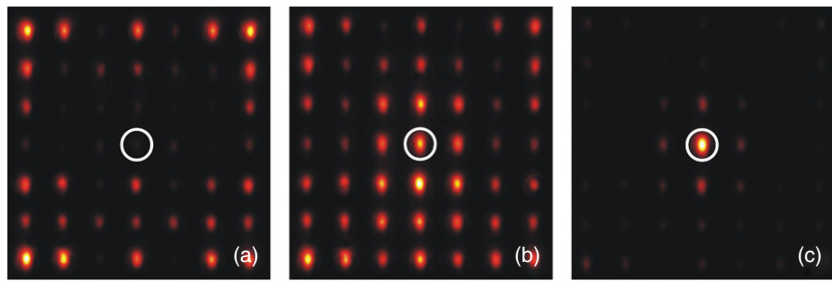


Figure 29. Formation of a 2D discrete soliton in the experiment. (a) Linear diffraction at $P_{\text{peak}} = 40 \text{ kW}$ input peak power. (b) At $P_{\text{peak}} = 1400 \text{ kW}$ a slightly localized intermediate state is observed. (c) For a peak power of $P_{\text{peak}} = 2000 \text{ kW}$, light is trapped in a single waveguide: a soliton has been formed. The sample was 105 mm long, the waveguide spacing was 40 μm and the fabrication was performed at 3 μJ pulse energy and 1250 $\mu\text{m s}^{-1}$ writing speed. The excited waveguides are marked with a white circle.

a discrete 2D soliton was accomplished in lattices optically induced in a photorefractive crystal [77]. This induction technique is today the most common method in the realization of 2D waveguide lattices [78]. However, in contrast the alternative approach based on the fs direct writing technique has some inherent advantages, including e.g. the insertion of artificial defects, the creation of anisotropic coupling, and the realization of boundaries and interfaces between different array topologies.

In the experiments for the observation of 2D solitons in fs-written waveguide arrays presented here, a square 7×7 lattice ($m, n = 1, \dots, 7$) was used with a sample length of 105 mm and a waveguide separation of 40 μm . The writing velocity was chosen to be 1250 $\mu\text{m s}^{-1}$. In order to avoid damage of the device when exciting with high-power laser pulses, the waveguides are buried 0.5 mm away from the incoupling facet as discussed above. The change in the discrete output pattern with increasing peak power is demonstrated in figure 29. In figure 29(a) the output pattern in the linear case at $P_{\text{peak}} = 40 \text{ kW}$ is shown. The linear coupling is only marginally influenced by the anisotropy (ellipticity) of the waveguides, since the waveguide separations are large, so the coupling is only weakly anisotropic. At $P_{\text{peak}} = 1400 \text{ kW}$ (see figure 29(b)) the linear coupling is reduced and at $P_{\text{peak}} = 2000 \text{ kW}$ (figure 29(c)), almost all of the guided energy remains in the excited waveguide: a 2D discrete soliton has been generated [79]. It is evident that the power required for soliton formation in a 2D lattice is usually considerably higher compared to the 1D case (for the same fabrication parameters). The explanation is simple: according to figure 25(a), the propagation constant of the excited waveguide has to be shifted out of the band in order to form a nonlinear isolated state. One can easily verify that the two-dimensional version of the dispersion relation equation (7) has a significantly larger width (see e.g. figures 31(b), (c)) than the 1D case (compare figure 25(a)), so a higher power is required to leave the band and move into the gap.

2D discrete solitons at surfaces and interfaces

The presence of an interface between materials with different physical properties can profoundly affect the evolution of nonlinear excitations. Such interfaces support specific

stationary excitations, which are called surface waves. These are encountered in various areas of physics including solid-state physics, near-surface optics, plasmas and acoustics [80–83]. In nonlinear optics, surface waves residing at the interface between naturally uniform materials typically are observed when their power exceeds a certain threshold and are stable under appropriate conditions [84]. However, the progress in their experimental observation was severely limited because of unrealistically high power levels required for a surface wave excitation at the interfaces of natural materials. Interestingly, it turned out that the relatively shallow refractive index modulation in waveguide arrays facilitates the formation of nonlinear optical surface waves significantly and they can be observed already at moderate power levels at the edge of semi-infinite arrays in the 1D [85, 86] as well as in the two-dimensional case [87–89].

The formation of discrete surface solitons is subject to somewhat different physical factors than for discrete solitons without any boundary interaction. Propagation bands and bandgaps are a direct consequence of the periodicity of an infinite waveguide array, yielding the existence of discrete solitons when the propagation constant of the travelling modes is shifted by the nonlinear influence from the bands into the bandgaps. The required periodicity is also approximately satisfied in a finite lattice, when the influence of the boundary on the propagation of the mode can be neglected. The situation completely changes in the presence of a surface, since the periodicity is abruptly interrupted. The former homogeneous band structure is splitting up depending on the distance to the surface, so the simplified picture of shifting the propagation constant from the band into the bandgap is no longer valid.

For the experiments shown here the same sample as for the 2D discrete soliton in the bulk of the array was used. The power-dependent transformation from linear diffraction to the discrete soliton is shown in figure 30 for the surface (left column) and the corner case (right column). At low input peak power $P_{\text{peak}} = 40 \text{ kW}$ the pattern broadens due to discrete diffraction, and all of the power in the excited waveguides has been coupled into the adjacent ones, as shown in figure 30(a). Increasing the power to $P_{\text{peak}} = 1800 \text{ kW}$ a slightly localized intermediate state is observed (figure 30(b)). Eventually, at $P_{\text{peak}} = 4800 \text{ kW}$ the light is almost completely ‘trapped’ in the form of a discrete soliton in the excited waveguide,

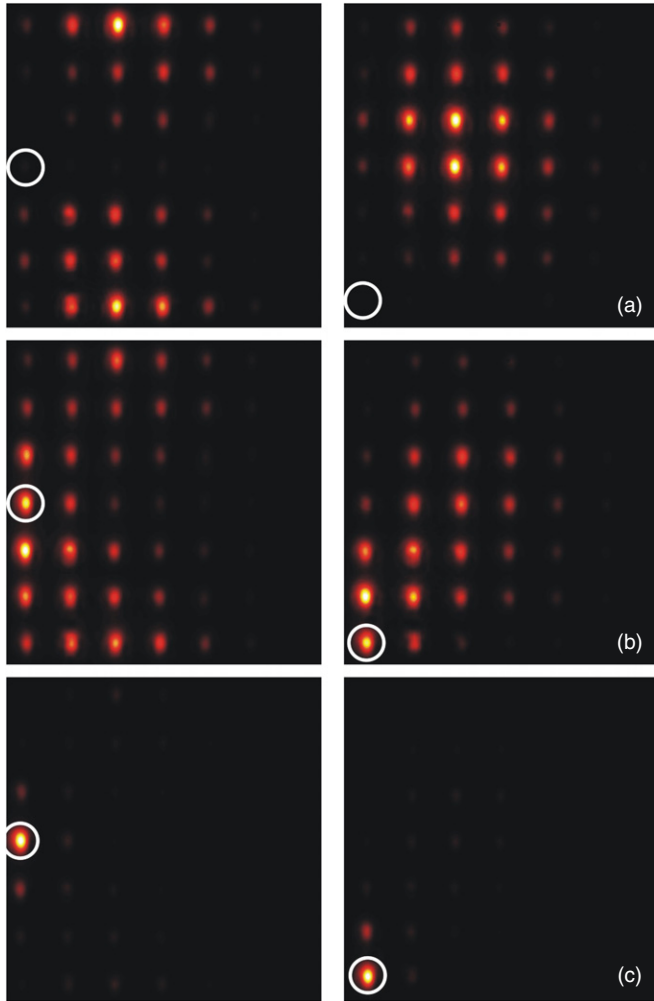


Figure 30. Excitation of a discrete surface (left column) and corner (right column) soliton. (a) Linear diffraction at $P_{\text{peak}} = 40 \text{ kW}$ input peak power. (b) At $P_{\text{peak}} = 1800 \text{ kW}$ a slightly localized intermediate state is observed. (c) For a peak power of $P_{\text{peak}} = 4800 \text{ kW}$, a soliton has been formed. The sample is the same as in figure 29. The excited waveguides are marked with a white circle.

corresponding to a stable nonlinear surface wave [89] (figure 30(c)). The required power for soliton formation at

the surface is considerably higher than in the bulk of the array. This is due to the repulsive character of the array surface [90], which the nonlinearity has to overcome in addition. The high accuracy of the writing process results in waveguide arrays which exhibit sharply defined boundaries. This ensures the absence of scattering or noticeable statistical distortions of the output pattern caused by small waveguide displacements or inhomogeneities and proves that the fs laser writing technique is ideally suited for studying surface phenomena.

Nonlinear surface waves are also possible at an interface between two dissimilar discrete media in 1D geometries [87, 91] as well as in 2D settings, e.g. at the interface between a square lattice and a hexagonal lattice [92] (see figure 31(a), where the interface is marked with a black dotted line). Importantly, the generalized dispersion relations (compare equation (7)) for the square lattice (figure 31(b)) and the hexagonal lattice (figure 31(c)) are different. Additionally, the hexagonal region exhibits a higher packing density of the waveguides, leading to a higher mean refractive index. In figure 32, a sequence of output intensity distributions is shown, which demonstrate the interplay of interface reflection, enhanced light penetration into the region with higher mean refractive index and nonlinear propagation. The sample was 105 mm long, and the spacing between adjacent guides was 40 μm in this case. Additionally, the refractive index of the individual guides in the hexagonal lattice is slightly higher, achieved by a slightly lower writing speed in this region ($1800 \mu\text{m s}^{-1}$), compared to the square region ($2000 \mu\text{m s}^{-1}$). When a waveguide in the first (interface) row of the square array is excited, for low peak power $P_{\text{peak}} = 40 \text{ kW}$ the light is almost confined to the square region since it is reflected at the interface (figure 32(a)). For increasing power the light starts to penetrate into the hexagonal region (figures 32(b) and (c)), for $P_{\text{peak}} = 1400 \text{ kW}$ and $P_{\text{peak}} = 2000 \text{ kW}$, respectively) because nonlinearity increases the refractive index and causes phase matching of both array sections. However, even for large input peak powers one can clearly observe near-interface localization (figures 32(d) ($P_{\text{peak}} = 2300 \text{ kW}$) and (e) ($P_{\text{peak}} = 2700 \text{ kW}$)), so that finally at $P_{\text{peak}} = 3200 \text{ kW}$ an interface lattice soliton forms (figure 32(f)). Note the reduced power threshold compared to the surface soliton case, which, however, is still higher than for 2D solitons in the array bulk.

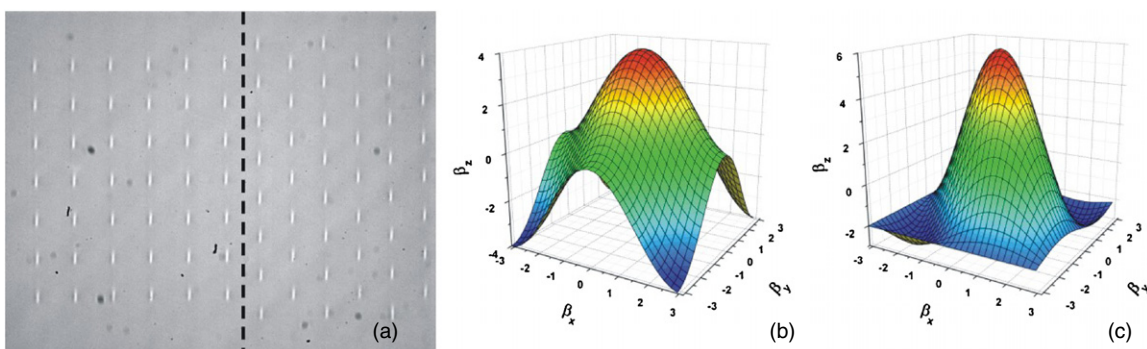


Figure 31. A sample for 2D discrete interface solitons. (a) A microscope image of the sample, where the left region exhibits a square geometry and the right region a hexagonal geometry. (b) The dispersion relation of a square lattice with only horizontal and vertical coupling. (c) The dispersion relation of a hexagonal lattice. Figures from [90].

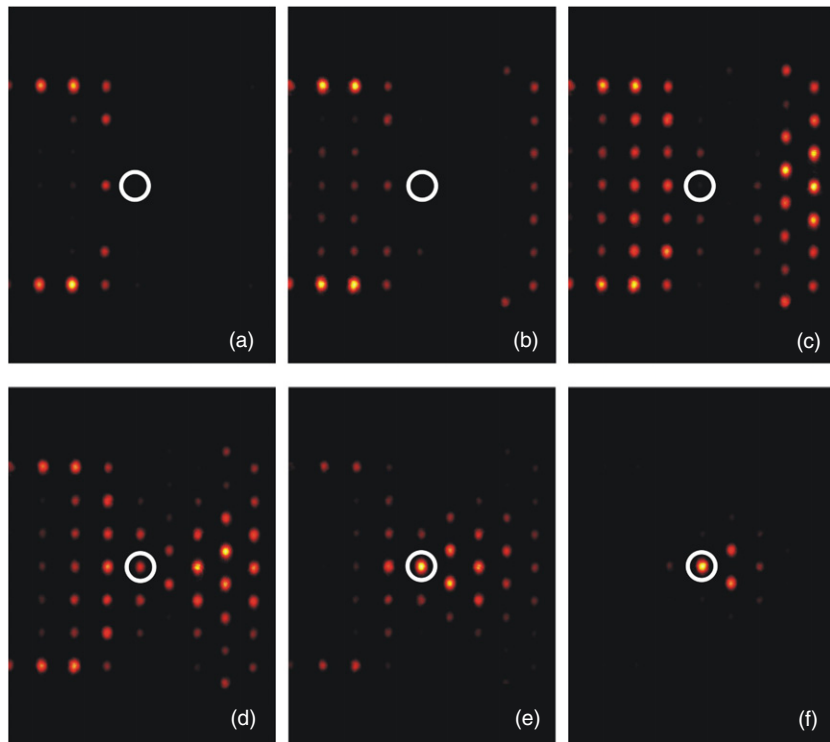


Figure 32. Different stages of the formation of a 2D discrete interface soliton in the experiment. The light was launched into a waveguide in the first row of the square array. The input power is (a) 62 kW, (b) 1.4 MW, (c) 2 MW, (d) 2.3 MW, (e) 2.7 MW and (f) 3.2 MW. The excited waveguides are marked with a white circle. Figures from [90].

The repulsive character of the interface is preserved but is much weaker than for a surface.

Conclusion

Arrays of optical waveguides provide an exceptional tool for studying various optical phenomena in the linear regime as well as in the nonlinear regime. Particularly, this so-called discrete optics has the potential to mimic many different quantum systems in a fully classical domain. The fs-laser-writing approach for the fabrication of waveguide arrays thereby exhibits a variety of advantages such as the stability and homogeneity of the waveguides and the evanescent coupling, the processing speed and the possibility of fabricating arbitrary 1D and 2D topologies for linear and nonlinear light propagation. Furthermore, it is possible to precisely control the properties of every single waveguide, to generate sharply defined surfaces or artificial defects. This allows analysis of the influence of boundary and interfacing effects, making fs-laser-written waveguide arrays today the only systems where complex two-dimensional interfaces can be realized [93]. The additional possibility of writing the waveguides along arbitrary paths with high precision allows the implementation of external potentials by curving the guides.

Although all examples in this tutorial have been restricted to fused silica, the fs writing technique allows us to process a variety of materials [94–97], which exhibit other kinds of nonlinearity, in particular a $\chi^{(2)}$ nonlinearity, as can be found e.g. in LiNbO₃ [98–100]. In order to obtain high nonlinear

efficiencies, a further extension to materials with tailored nonlinear response such as periodically poled LiNbO₃ [101] is also a very promising approach. The experimental focus will be on the precise control of the waveguide properties in these media, including the handling of spherical aberrations, which is important for the fabrication of 2D geometries.

To summarize, it was demonstrated that fabricating complex refractive index landscapes with the fs laser-writing approach has a variety of advantages leaving these structures as an important alternative to common fabrication techniques. Due to the diversity of topologies which are realizable, the multiple degrees of freedom and the high temporal stability of the waveguides, in a couple of years the fs-laser-writing technique may become a major technique for the fabrication of integrated optical devices. Owing to the unique properties of the discrete propagation of light, all-optical switching and routing devices will progress from theoretical considerations to real-world applications in numerous operational areas.

Acknowledgments

The authors would like to thank the Leopoldina, the German Academy of Science (grant LDPS 2009-13), the Jenoptik AG and the Deutsche Forschungsgemeinschaft (Leibniz program and Research Unit 532 ‘Nonlinear spatio-temporal dynamics in dissipative and discrete optical systems’) for funding this work. Support of, and discussion with, F Dreisow, M Heinrich, R Keil, A Tünnermann, T Pertsch and M Segev are gratefully acknowledged.

References

- [1] Longhi S 2008 Quantum-optical analogies using photonic structure *Laser Photonics Rev.* **3** 243–61
- [2] Christodoulides D N, Lederer F and Silberberg Y 2003 Discretizing light behaviour in linear and nonlinear optical waveguide lattices *Nature* **424** 817–23
- [3] Efremidis N, Hudock J, Christodoulides D, Fleischer J, Cohen O and Segev M 2003 Two-dimensional optical lattice solitons *Phys. Rev. Lett.* **92** 213906
- [4] Fleischer J, Segev M, Efremidis N and Christodoulides D N 2003 Observation of two-dimensional discrete solitons in optically induced nonlinear photonic lattices *Nature* **422** 147–50
- [5] Lederer F, Stegeman G I, Christodoulides D N, Assanto G, Segev M and Silberberg Y 2009 Discrete solitons in optics *Phys. Rep.* **463** 1–126
- [6] Pertsch T, Peschel U, Lederer F, Burghoff J, Will M, Nolte S and Tünnermann A 2004 Discrete diffraction in two-dimensional arrays of coupled waveguides in silica *Opt. Lett.* **29** 468–70
- [7] Itoh K, Watanabe W, Nolte S and Schaffer C 2006 Ultrafast processes for bulk modification of transparent materials *MRS Bull.* **31** 620–5
- [8] Eisenberg H S, Silberberg Y, Morandotti R and Aitchison J S 2000 Diffraction management *Phys. Rev. Lett.* **85** 1863–6
- [9] Pertsch T, Zentgraf T, Peschel U, Braeuer A and Lederer F 2002 Anomalous refraction and diffraction in discrete optical systems *Phys. Rev. Lett.* **88** 093901
- [10] Mandelik D, Eisenberg H S, Silberberg Y, Morandotti R and Aitchison J S 2003 Band-gap structure of waveguide arrays and excitation of Floquet–Bloch solitons *Phys. Rev. Lett.* **90** 053902
- [11] Yariv A 1991 *Optical Electronics* 4th edn (Philadelphia, PA: Saunders)
- [12] Russel P S J 1986 Optics of Floquet–Bloch waves in dielectric gratings *Appl. Phys. B* **39** 231–46
- [13] Szameit A, Pertsch T, Dreisow F, Nolte S, Tünnermann A, Peschel U and Lederer F 2007 Light evolution in arbitrary two-dimensional waveguide arrays *Phys. Rev. A* **75** 053814
- [14] Chan J, Huser T, Risbud S and Krol D 2001 Structural changes in fused silica after exposure to focused femtosecond laser pulses *Opt. Lett.* **26** 1726–8
- [15] Streltsov A and Borelli N 2002 Study of femtosecond-laser-written waveguides in glasses *J. Opt. Soc. Am. B* **19** 2496–504
- [16] Miura K, Qui J, Inoue H, Mitsuyu T and Hirao K 1997 Photowritten optical waveguides in various glasses with ultrashort pulse laser *Appl. Phys. Lett.* **71** 3329–31
- [17] Nolte S, Will M, Burghoff J and Tünnermann A 2003 Femtosecond waveguide writing a new avenue to three-dimensional integrated optics *Appl. Phys. A* **77** 109–11
- [18] Itoh K, Watanabe W, Nolte S and Schaffer C B 2006 Ultrafast processes for bulk modification of transparent materials *MRS Bull.* **31** 620–5
- [19] Gattass R R and Mazur E 2008 Femtosecond laser micromachining in transparent materials *Nat. Photonics* **2** 219–25
- [20] Della Valle G, Osellame R and Laporta P 2009 Micromachining of photonic devices by femtosecond laser pulses *J. Opt. A* **11** 013001
- [21] Ams M, Marshall G D, Dekker P, Piper J A and Withford M J 2009 Ultrafast laser written active devices *Laser Photonics Rev.* **3** 535–44
- [22] Mansour I and Caccavale F 1996 An improved procedure to calculate the refractive index profile from the measured near-field intensity *J. Lightwave Technol.* **14** 423–8
- [23] Blömer D, Szameit A, Dreisow F, Schreiber T, Nolte S and Tünnermann A 2006 Nonlinear refractive index of fs-laser-written waveguides in fused silica *Opt. Express* **14** 2151–7
- [24] Szameit A, Dreisow F, Hartung H, Nolte S and Tünnermann A 2007 Quasi-incoherent propagation in waveguide arrays *Appl. Phys. Lett.* **90** 241113
- [25] Dreisow F, Heinrich M, Szameit A, Doering S, Nolte S, Tünnermann A, Fahr S and Lederer F 2008 Spectral resolved dynamic localization in curved fs laser written waveguide arrays *Opt. Express* **14** 3474–83
- [26] Skuja L, Suzuki T and Tanimura K 1995 Site-selective laser-spectroscopy studies of the intrinsic 1.9-eV luminescence center in glassy SiO₂ *Phys. Rev. B* **52** 15208–16
- [27] Stevens-Kalceff M, Stesmans A and Wong J 2002 Defects induced in fused silica by high fluence ultraviolet laser pulses at 355 nm *Appl. Phys. Lett.* **80** 758–60
- [28] Trompeter H, Pertsch T, Lederer F, Michaelis D, Streppel U, Bräuer A and Peschel U 2006 Visual observation of Zener tunneling *Phys. Rev. Lett.* **96** 023901
- [29] Bloch F 1928 Über die Quantenmechanik der Elektronen in Kristallgittern *Z. Phys.* **52** 555–600
- [30] Feldmann J, Leo K, Shah J, Miller D, Cunningham J, Meier T, von Plessen G, Schulze A, Thomas P and Schmitt-Rink S 1992 Optical investigation of Bloch oscillations in a semiconductor superlattice *Phys. Rev. B* **46** 7252–5
- [31] Nenciu G 1991 Dynamics of band electrons in electric and magnetic fields: rigorous justification of the effective Hamiltonians *Rev. Mod. Phys.* **63** 91–127
- [32] Lenz G, Talanina I and de Sterke M 1999 Bloch oscillations in an array of curved optical waveguides *Phys. Rev. Lett.* **83** 963–6
- [33] Longhi S 2005 Self-imaging and modulational instability in an array of periodically curved waveguides *Opt. Lett.* **30** 2137–9
- [34] Peschel U, Pertsch T and Lederer F 1998 Optical Bloch oscillations in waveguide arrays *Opt. Lett.* **23** 1701–3
- [35] Longhi S 2006 Optical Zener–Bloch oscillations in binary waveguide arrays *Europhys. Lett.* **76** 416–21
- [36] Pertsch T, Dannberg P, Elflein W, Braeuer A and Lederer F 1999 Optical Bloch oscillations in temperature tuned waveguide arrays *Phys. Rev. Lett.* **83** 4752–5
- [37] Morandotti R, Peschel U, Aitchinson J S, Eisenberg H S and Silberberg Y 1999 Experimental observation of linear and nonlinear optical Bloch oscillations *Phys. Rev. Lett.* **83** 4756–9
- [38] Usievich B A, Sychugov V A, Nirligareev J Kh and Golant K M 2004 A circular system of coupled waveguides and an optical analogue of Bloch oscillations *Opt. Spectrosc.* **97** 790–5
- [39] Chiodo N, Valle G D, Osellame R, Longhi S, Cerullo G, Ramponi R, Laporta P and Morgner U 2006 Imaging of Bloch oscillations in erbium-doped curved waveguide arrays *Opt. Lett.* **31** 1651–3
- [40] Dreisow F, Szameit A, Heinrich M, Pertsch T, Nolte S, Tünnermann A and Longhi S 2009 Bloch–Zener oscillations in binary superlattices *Phys. Rev. Lett.* **102** 076802
- [41] Trompeter H, Pertsch T, Lederer F, Michaelis D, Streppel U, Braeuer A and Peschel U 2006 Visual observation of Zener tunneling *Phys. Rev. Lett.* **96** 023901
- [42] Zener C 1934 A theory of the electrical breakdown of solid dielectrics *Proc. R. Soc. A* **145** 523–9
- [43] Dunlap D and Kenkre V 1986 Dynamic localization of a charged particle moving under the influence of an electric field *Phys. Rev. B* **34** 3625–33

- [44] Tsu R and Esaki L 1973 Tunneling in a finite superlattice *Appl. Phys. Lett.* **22** 562–4
- [45] Holthaus M 1992 Collapse of minibands in far-infrared irradiated superlattices *Phys. Rev. Lett.* **69** 351–4
- [46] Madureira J R, Schulz P A and Maialle M Z 2004 Dynamic localization in finite quantum-dot superlattices: A pure ac field effect *Phys. Rev. B* **70** 033309
- [47] Longhi S, Marangoni M, Lobino M, Ramponi R, Laporta P, Cianci E and Foglietti V 2006 Observation of dynamic localization in periodically curved waveguide arrays *Phys. Rev. Lett.* **96** 243901
- [48] Iyer R, Aitchison J, Wan J, Dignam M and de Sterke M 2007 Exact dynamic localization in curved AlGaAs optical waveguide arrays *Opt. Exp.* **15** 3212–23
- [49] Szameit A, Pertsch T, Nolte S, Tünnermann A and Lederer F 2008 Long-range interaction in waveguide lattices *Phys. Rev. A* **77** 043804
- [50] Dreisow F, Szameit A, Heinrich M, Pertsch T, Nolte S and Tünnermann A 2008 Second order coupling in femtosecond laser written waveguide arrays *Opt. Lett.* **33** 2689–91
- [51] Patorski K. 1989 The self-imaging phenomenon and its applications *Prog. Opt.* **27** 3–108
- [52] Soldano L and Pennings E 1995 Optical multi-mode interference devices based on self-imaging: principles and applications *J. Lightwave Technol.* **13** 615–27
- [53] Hudson D, Shish K, Schibli T, Kutz N, Christodoulides D N, Morandotti R and Cundiff S T 2008 Nonlinear femtosecond pulse reshaping in waveguide arrays *Opt. Lett.* **33** 1440–2
- [54] Bryngdahl O 1973 Image formation using self-imaging techniques *J. Opt. Soc. Am.* **63** 416–9
- [55] Iwanow R, May-Arrioja D A, Christodoulides D N, Stegeman G I, Min Y and Sohler W 2005 Discrete Talbot effect in waveguide arrays *Phys. Rev. Lett.* **95** 053902
- [56] Garanovich I L, Szameit A, Sukhorukov A A, Pertsch T, Krolikowski W, Nolte S, Neshev D, Tünnermann A and Kivshar Y S 2007 Diffraction control in periodically curved two-dimensional waveguide arrays *Opt. Express* **15** 9737–47
- [57] Szameit A, Garanovich I L, Heinrich M, Sukhorukov A A, Dreisow F, Pertsch T, Nolte S, Tünnermann A and Kivshar Y S 2009 Polychromatic dynamic localization in curved photonic lattices *Nat. Phys.* **5** 271–5
- [58] Longhi S 2009 Polychromatic optical Bloch oscillations *Opt. Lett.* **34** 2174–6
- [59] Gordon R 2004 Harmonic oscillation in a spatially finite array waveguide *Opt. Lett.* **29** 2752–4
- [60] Longhi S 2008 Image reconstruction in segmented waveguide arrays *Opt. Lett.* **33** 473–5
- [61] Szameit A, Dreisow F, Heinrich M, Pertsch T, Nolte S, Tünnermann A, Suran E, Louradour F, Barthelemy A and Longhi S 2008 Image reconstruction in segmented femtosecond laser-written waveguide arrays *Appl. Phys. Lett.* **93** 181109
- [62] Frenkel J and Kontorova T 1939 On the theory of plastic deformation and swimming *J. Phys. (USSR)* **1** 137–49
- [63] Davydov A 1977 Solitons and energy transfer along protein molecules *J. Theor. Biol.* **66** 379–87
- [64] Jensen S 1982 The nonlinear coherent coupler *IEEE J. Quantum Electron.* **18** 1580–3
- [65] Christodoulides D N and Joseph R I 1988 Discrete self-focusing in nonlinear arrays of coupled waveguides *Opt. Lett.* **13** 794–6
- [66] Eisenberg H S, Silberberg Y, Morandotti R, Boyd A and Aitchison J S 1998 Discrete spatial optical solitons in waveguide arrays *Phys. Rev. Lett.* **81** 3383–6
- [67] Lederer F and Silberberg Y 2002 Discrete solitons *Opt. Photonics News* **13** 48–53
- [68] Milam D 1998 Review and assessment of measured values of the nonlinear refractive index coefficient of fused silica *Appl. Opt.* **37** 546–50
- [69] Zoubir A, Richardson M, Canioni L, Brocas A and Sarger L 2005 Optical properties of IR femtosecond laser-modified fused silica and application to waveguide fabrication *J. Opt. Soc. Am. B* **22** 2138–43
- [70] Chiao R, Garmire E and Townes C 1964 Self-trapping of optical beams *Phys. Rev. Lett.* **13** 479–82
- [71] Barthelemy A, Maneuf S and Froehly C 1985 Soliton propagation and self-trapping of laser beams by a Kerr optical nonlinearity *Opt. Commun.* **55** 201–6
- [72] Fleischer J W, Carmon T, Segev M, Efremidis N K and Christodoulides D N 2003 Observation of discrete solitons in optically induced real time waveguide arrays *Phys. Rev. Lett.* **90** 023902
- [73] Szameit A, Blömer D, Burghoff J, Schreiber T, Pertsch T, Nolte S, Tünnermann A and Lederer F 2005 Discrete nonlinear localization in femtosecond laser written waveguides in fused silica *Opt. Express* **13** 10552–7
- [74] Garanovich I L, Sukhorukov A A and Kivshar Y S 2007 Nonlinear diffusion and beam self-trapping in diffraction-managed waveguide arrays *Opt. Express* **15** 9547–52
- [75] Szameit A *et al* 2008 Observation of diffraction-managed discrete solitons in curved waveguide arrays *Phys. Rev. A* **78** 031801
- [76] Kelley P L 1965 Self-focusing of optical beams *Phys. Rev. Lett.* **15** 1005–8
- [77] Fleischer J W, Segev M, Efremidis N K and Christodoulides D N 2003 Observation of two-dimensional discrete solitons in optically induced nonlinear photonic lattices *Nature* **422** 147–50
- [78] Fleischer J W, Bartal G, Cohen O, Schwartz T, Manela O, Freedman B, Segev M, Buljan H and Efremidis N K 2005 Spatial photonics in nonlinear waveguide arrays *Opt. Express* **13** 1780–96
- [79] Szameit A, Burghoff J, Pertsch T, Nolte S, Tünnermann A and Lederer F 2006 Two-dimensional soliton in cubic fs laser written waveguide arrays in fused silica *Opt. Express* **14** 6055–62
- [80] Boardman A D, Bertolotti M and Twardowski T 1989 *Nonlinear Waves in Solid State Physics NATO Advanced Study Institutes Vol. 247* (New York: Plenum)
- [81] S and Kawata 2001 *Near-Field Optics and Surface Plasmon Polaritons* (Berlin: Springer)
- [82] Aliev Y M, Schluter H and Shivarova A 2000 *Guided-Wave-Produced Plasmas* (Berlin: Springer)
- [83] Biryukov S V, Gulyaev Y V, Krylov V V and Plessky V P 1995 *Surface Acoustic Waves in Inhomogeneous Media* (Berlin: Springer)
- [84] Mihalache D, Bertolotti M and Sibilia C 1989 Nonlinear wave propagation in planar structures *Prog. Opt.* **27** 229–313
- [85] Makris K G, Suntoev S, Christodoulides D N and Stegeman G I 2005 Discrete surface solitons *Opt. Lett.* **30** 2466–8
- [86] Suntoev S, Makris K G, Christodoulides D N, Stegeman G I, Hache A, Morandotti R, Yang H, Salamo G and Sorel M 2006 Observation of discrete surface solitons *Phys. Rev. Lett.* **96** 063901
- [87] Makris K G, Hudock J, Christodoulides D N, Stegeman G I, Manela O and Segev M 2006 Surface lattice solitons *Opt. Lett.* **31** 2774–6
- [88] Wang X, Bezryadina A, Chen Z, Makris K G, Christodoulides D N and Stegeman G I 2007 Observation of two-dimensional surface solitons *Phys. Rev. Lett.* **98** 123903
- [89] Szameit A, Kartashov Y, Dreisow F, Pertsch T, Nolte S, Tünnermann A and Torner L 2007 Observation of

- two-dimensional surface solitons in asymmetric waveguide arrays *Phys. Rev. Lett.* **98** 173903
- [90] Molina M I, Vicencio R A and Kivshar Y S 2006 Discrete solitons and nonlinear surface modes in semi-infinite waveguide arrays *Opt. Lett.* **31** 1693–5
- [91] Suntsov S, Makris K G, Christodoulides D N, Stegeman G I, Morandotti R, Volatier M, Aimez V, Ares R, Rüter C E and Kip D 2007 Optical modes at the interface between two dissimilar discrete meta-materials *Opt. Express* **15** 4663–70
- [92] Szameit A, Kartashov Y V, Dreisow F, Heinrich M, Vysloukh V A, Pertsch T, Nolte S, Tünnermann A, Lederer F and Torner L 2008 Observation of two-dimensional lattice interface solitons *Opt. Lett.* **33** 663–5
- [93] Szameit A, Kartashov Y V, Vysloukh V A, Heinrich M, Dreisow F, Pertsch T, Nolte S, Tünnermann A, Lederer F and Torner L 2008 Angular surface solitons in sectorial hexagonal arrays *Opt. Lett.* **33** 1542–4
- [94] Zoubir A, Lopez C, Richardson M and Richardson K 2004 Femtosecond laser fabrication of tubular waveguides in PMMA *Opt. Lett.* **29** 1840–2
- [95] Nejadmalayeri A, Herman P, Burghoff J, Will M, Nolte S and Tünnermann A 2005 Inscription of optical waveguides in crystalline silicon by mid-infrared femtosecond laser pulses *Opt. Lett.* **30** 964–6
- [96] Nandi P, Jose G, Jayakrishnan C, Debbarma S, Chalapathi K, Alti A D K, Dharmadhikari J and Mathur D 2006 Femtosecond laser written channel waveguides in tellurite glass *Opt. Express* **14** 12145–50
- [97] Hughes M, Yang W and Hewak D 2007 Fabrication and characterization of femtosecond laser written waveguides in chalcogenide glass *Appl. Phys. Lett.* **90** 131113
- [98] Gui L, Xu B and Chong T C 2004 Microstructure in lithium niobate by use of focused femtosecond laser pulses *IEEE Photon. Technol. Lett.* **16** 1337–9
- [99] Burghoff J, Grebing C, Nolte S and Tünnermann A 2006 Efficient frequency doubling in femtosecond laser-written waveguides in lithium niobate *Appl. Phys. Lett.* **89** 081108
- [100] Heinrich M, Szameit A, Dreisow F, Döring S, Thomas J, Nolte S, Tünnermann A and Ancona A 2008 Discrete diffraction in type-2 LiNbO₃ waveguide arrays *Appl. Phys. Lett.* **93** 101111
- [101] Thomas J, Heinrich M, Burghoff J, Nolte S, Ancona A and Tünnermann A 2007 Femtosecond laser-written quasi-phase-matched waveguides in lithium niobate *Appl. Phys. Lett.* **91** 151108